

UC Irvine

UC Irvine Electronic Theses and Dissertations

Title

Synthesis of 3D Bicontinuous Cu-Ni Alloy Scaffolds for Controlled Growth of Turbostratic Graphene

Permalink

<https://escholarship.org/uc/item/9cm7w9w5>

Author

Zhang, Zhengyu

Publication Date

2019

Peer reviewed|Thesis/dissertation

UNIVERSITY OF CALIFORNIA,
IRVINE

Synthesis of 3D Bicontinuous Cu-Ni Alloy Scaffolds for Controlled Growth of Turbostratic
Graphene

THESIS

submitted in partial satisfaction of the requirements
for the degree of

MASTER OF SCIENCE

in Materials Science and Engineering

by

Zhengyu Zhang

Thesis Committee:
Professor Regina Ragan, Chair
Professor Daniel Mumm
Professor Tim Rupert

2019

DEDICATION

To

my parents and friends

in recognition of their worth

Thanks for the guidance from Professor Regina Ragan

TABLE OF CONTENTS

	Page
LIST OF FIGURES	iv
LIST OF TABLES	v
ACKNOWLEDGMENTS	vi
ABSTRACT OF THE THESIS	vii
CHAPTER 1: Introduction	1
1.1 Motivation of current study	1
1.2 Current state of knowledge	3
CHAPTER 2: Synthesis of Cu-Ni alloy from bijel template	17
2.1 Motivation and background	17
2.2 Experiment method	19
2.3 Characterization	28
2.4 Conclusion	30
CHAPTER 3: CVD graphene growth on bi-CuNi	31
3.1 Introduction of thickness controlling method	31
3.2 Experiment method	33
3.3 Conclusion	37
CHAPTER 4: Summary and future work from the thesis	39
4.1 Summary of the thesis	39
4.1 Future directions	40
REFERENCES	42

LIST OF FIGURES

	page
Figure 1.1	Schematic of structural models of graphene/metal oxide composites 6
Figure 1.2	Schematic diagram for the 3D graphene fabrication 7
Figure 1.3	SEM image and illustration of gas-sensing 3D graphene 9
Figure 1.4	Two ways of approaching graphene 10
Figure 1.5	SEM of graphene from polymer template 11
Figure 1.6	Schematic diagrams of thermal CVD processes 13
Figure 1.7	Growth kinetics in CVD-produced graphene on various catalyst 14
Figure 1.8	Schematics of the CVD growth of uniform graphene over a Cu-Ni alloy film 15
Figure 1.9	Illustration of Bernal stacking graphene and Turbostratic stacking graphene 16
Figure 2.1	Examples of bicontinuous structures. 18
Figure 2.2	SEM of etched biNi 21
Figure 2.3	biNi before and after been etched 22
Figure 2.4	Illustration of the four steps for one cycle of electroless Cu deposition 23
Figure 2.5	SEM of bi-CuNi and biNi 24
Figure 2.6	Diagram of Cu electroless deposition 25
Figure 2.7	Relationship of Cu thickness with temperature and hole size 27
Figure 2.8	SEM and EDS data on different metal template 29
Figure 2.9	SEM image on different metal template 30
Figure 3.1	The relationship between I_{2D} FWHM and turbostratic graphene 33
Figure 3.2	SEM image on graphene and metal templates 34
Figure 3.3	Raman spectra analysis histograms on bi-CuNi-3DG 36
Figure 3.4	Raman spectra analysis histograms of biNi-3DG 37
Figure 4.1	Graphene grown from 71.76 weight% bi-CuNi, morphology lost 41

LIST OF TABLES

	Page
Table 2.1 Relationship between temperature and CuSO_4 solution density and CuSO_4 solubility	26

ACKNOWLEDGMENTS

I would like to express the deepest appreciation to my committee chair, Professor Regina Ragan, who has the attitude and the substance of a genius: she continually and convincingly conveyed a spirit of adventure in regarding to research, and an excitement in regard to teaching. Without her guidance and persistent help this dissertation would not have been possible.

I would like to thank my committee members, Professor Daniel Mumm and Professor Tim Rupert, I have taken their classes during my study in UCI, which give me great help in understanding basic knowledge of Materials Science.

ABSTRACT OF THE THESIS

Synthesis of 3D Bicontinuous Cu-Ni Alloy Scaffolds for Controlled Growth of Turbostratic Graphene

By

Zhengyu Zhang

Master of Science in Materials Science and Engineering

University of California, Irvine, 2019

Professor Regina Ragan, Chair

3-dimensional (3D) porous graphene is a promising platform for applications such as catalysis, sensors, and energy storage. In this thesis, bicontinuous interfacially jammed emulsion gel (bijel) templates are formed and chemically and thermally processed into sacrificial porous Cu-Ni alloy scaffolds which in turn are used for chemical vapor deposition (CVD) of graphene. Metal scaffolds formed from the bijel structure have large specific surface area and inherit the co-continuous property from their parent bijel. However, graphene grown via CVD on bicontinuous nickel scaffolds (biNi) will typically produce thick graphene layers due to the high carbon solubility in Ni unless the CVD growth is limited to short growth times of a few seconds. In the latter case, number of layers may be variable across the sample due to difficulties in controlling deposition kinetics in short growth times. In addition, thick graphite layers may form in the Ni grain boundaries leading to highly non uniform number of layers in 3D samples. Previous reports have shown that the number of layers and uniformity of CVD graphene can be controlled when using the Cu-Ni alloys as scaffolds. In this case, research has been limited to CVD growth on 2-dimensional Cu-Ni alloy surfaces. Here, in this thesis, the fabrication of 3D bicontinuous Cu-Ni alloy metal scaffolds(bi-CuNi) are successfully achieved. By varying electrochemical processing

parameters, bi-CuNi with porous morphology containing 46.8% and 35.8% Cu in weight percentage are produced. When comparing the morphology and number of layers of resultant CVD graphene growth on the alloy scaffolds using the same CVD growth parameters on both samples, Raman spectroscopy measurements show many regions with a high 2D mode intensity with the higher Cu alloy concentration in the scaffold. Raman analysis showing that 3D graphene from bi-CuNi via CVD (bi-CuNi-3DG) exhibits turbostratic stacking in many regions of the sample. Turbostratic graphene can exhibit similar properties as single-layer graphene (SLG), indicating that emphasis on tuning physical properties of scaffold alloys has promise to yield 3D graphene structures with excellent electronic properties. In future work, precise control of Cu concentration in bi-CuNi is expected to control both graphene layer number and stacking, and thereby the electronic properties of the resultant 3D graphene architectures for numerous applications.

Chapter 1

Introduction

1.1 Motivation of present study

The present study aims to produce bicontinuous 3-dimensional (3D) Cu-Ni alloy metal scaffolds (bi-CuNi) for graphene growth. After the chemical vapor deposition (CVD) process, 3D porous graphene from bi-CuNi (bi-CuNi-3DG) is formed. Furthermore, two reasons motivate the present work: (1) the bicontinuous 3D porous graphene with large specific surface area and high electrical conductivity holds great potential in many electronic applications [5, 6, 58]; (2) the use of the CVD technique and bi-CuNi with bicontinuous structure inherited from bicontinuous interfacially jammed emulsion gel (bijel) holds promise in making 3D porous graphene that has both excellent electronic properties and bicontinuous structure [17].

1.1.1 Motivation: making a 3D porous structure graphene

3D porous graphene, if manufactured with proper layer stacking and number of layers, can have high electrical conductivity and large specific surface area, which holds great potential to be used in many applications after having been functionalized [5, 6, 58]. For example, in energy storage, after being coated with Co_3O_4 , the 3D porous graphene can become electrochemical capacitors with high specific capacitance and excellent cycling stability [5, 77]; in catalysis, after being doped with nitrogen, the 3D porous graphene can be a highly efficient oxygen reduction reaction (ORR) catalyst [58]; in sensors, after being deposited with bismuth on the surface, the 3D porous graphene can be a sensitive sensor for heavy metal ion detection [6].

Due to the unique structure of 3D porous graphene, which is that of graphene sheets arranged in the 3D porous structure, it has interconnected 2D graphene sheets that ensure high electrical conductivity, and intrinsic large specific surface area provided by a porous structure [1–4].

1.1.2 Motivation: CVD of graphene on bicontinuous Cu-Ni alloy scaffolds

The goal is to use chemical vapor deposition (CVD) on bicontinuous Cu-Ni alloy template (bi-CuNi) to form 3D porous graphene with high electrical conductivity and large specific surface area.

The use of the CVD technique can help achieve the electrical and mechanical properties of graphene observed in 2D films [9, 26], i.e., layers of graphene with low defect density [7] and excellent electronic properties [8]. For example, a sheet resistance as low as $\sim 280 \Omega \text{ cm}^{-2}$ and carrier mobility as high as $3,700 \text{ cm}^2 \text{ V}^{-1} \text{ s}^{-1}$ has been observed [9]. It is reported that the number of layers and uniformity of CVD graphene can be controlled by the use of Cu-Ni alloy in CVD growth on 2D films [28]. Therefore, through the inspiration of the idea of using 2D Cu-Ni alloy films in CVD, the method of manufacturing 3D porous Cu-Ni alloy scaffolds is studied in this thesis. The number of layers of the graphene is related to the carbon solubility of the metal template used in CVD. On the Cu scaffolds, the low solubility of carbon helps the graphene growth process become self-limiting, and the single-layer graphene with a small percentage (less than 5%) of the area with a few layers is observed [10]. Metals such as Ni have a high carbon solubility, which tend to form thick graphite on grain boundaries [11]. Therefore, Ni scaffolds find it hard to yield uniform graphene layers, but always end up with a wide variation in number of layers over the metal surface from monolayer to many layers [9, 12]. Since Cu and Ni are well-known isomorphous systems, the Cu-Ni alloy would be an ideal system that has moderate and controllable carbon solubility by tuning the atomic fraction of Ni in Cu.

The bicontinuous porous metal scaffolds are synthesized from bijel and can ensure the CVD graphene with bicontinuous porous structure and large specific surface area [17]. The continuous void space afforded by bijel templates means that the entire internal surface area is readily accessible to the analyte solution, providing advanced transport and electrochemical properties [17–19]. As mentioned above, 3D porous graphene is a promising platform for applications such as energy storage, catalysis, and sensors [5, 6, 58]. The commercially produced sponge-like porous Ni template is widely used as a metal precursor in CVD to approach a porous structured graphene [14–16], but with limited surface area, limited control over pore (100 μm), and ligament size distribution when compared to Ni scaffolds synthesized from bijel templates [5, 16, 65, 66].

1.2 Current state of knowledge

1.2.1 Introduction to 3-dimensional (3D) porous structure graphene

2D graphene sheets can be assembled into 3D porous graphene and work as a promising platform for applications such as energy storage [5, 56], catalysis [20, 58], and sensors [6, 59, 60] as mentioned before. It is well known that graphene is one of the stiffest and strongest materials with high electrical conductivity, which can provide fast charge transfer rate for electrochemical reactions occurring at the graphene/solution or graphene/gas interface [46, 47, 59, 60]. Although single layer graphene is an ideal platform for engineering applications of electronic devices, a single layer of 2D graphene is too delicate to be used in a 3D architecture [48–50]. On the other hand, 3D porous graphene is easy to be functionalized and can be optimized for the applications mentioned above, with its inherent high stiffness, strength, electrical conductivity of the material, and large specific surface area provided by the architecture [5, 11, 17]. Moreover, theoretical calculations have predicted that 3D porous graphene can even be lighter than air, with

mechanical properties strong enough for applications under extreme conditions such as being a substitute for helium in filling up an unpowered balloon [51]. 3D porous graphene architectures are thus desirable and when structures are optimized as they can exhibit outstanding mechanical, thermal and electrical properties, with greater promise for making lighter and stronger products, playing a profound game-changing role in broad industrial areas [51].

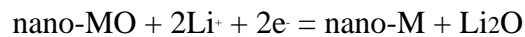
Different 3D graphene manufacturing techniques will have a huge influence on the properties of graphene and its performance in applications [9, 21–25]. Typical manufacturing techniques include the assembling of graphene oxide to 3D structure and reduction [21, 22], and chemical vapor deposition (CVD) on metal scaffolds [9, 23–25]. Of these, CVD has always been considered a reliable method to produce graphene 2D films with low defect density and high electrical conductivity [24, 25].

When synthesizing both 2D and 3D graphene, differences in number of layers and layer stacking orientation have huge influence on the electronic and mechanical properties of 3D porous graphene. Thus it is important to have a reliable fabrication method to control both number of layers and relative orientation [10, 27, 42, 43, 51]. The number of layers of the CVD graphene on 2D films can vary substantially, from monolayer to more than eight layers on different films, such as Ni [33], Cu [10], and Cu-Ni alloy [28], but most 3D porous graphene only use Ni scaffolds and have much thicker layers [16, 75, 76]. It is reported that the number of layers of graphene can be controlled when using Cu-Ni alloy, but existing work has mainly been limited to 2D films [28, 61]. In 3D porous graphene, the relative crystalline orientation between layers, which is called stacking mode of multiple-layer graphene (MLG) is complicated, including the Bernal stacking graphene and turbostratic stacking graphene [42]. Bernal stacked (or ABA stacked) graphene, where half of the atoms lie over the center of a hexagon in the lower

graphene sheet and half of atoms lie over an atom, has poor electronic properties when the number of layers is greater than 4 [80], whereas the turbostratic graphene can exhibit similar properties as single-layer graphene (SLG), including high electronic conductivity [42, 43]. It is important to characterize the stacking mode in 3D porous graphene in order to understand fabrication methods that produce graphene with more turbostratic stacking.

1.2.2 3D porous graphene applications in energy storage

In order to develop energy storage devices with high power and energy densities, electrodes should be able to provide a fast pathway for efficient ionic and electronic transport [52]. As mentioned above, 3D porous graphene can meet these requirements after being functionalized [5, 11, 17] and controlling layer thickness and stacking mode. Much effort has involved the use of 3D porous graphene as a platform in energy storage applications. At present, commercial graphite anode in Li-ion batteries have limited specific capacity and hard to meet the increasing demand for Li-ion batteries with high energy density; active materials anode such as metal oxides can have good specific capacity, but with problems like volume expansion and poor electrical conductivity. However, 3D graphene, after been functionalized with active materials, can have good electrical conductivity and high specific capacity [78]. In many cases, 3D porous graphene is often functionalized with a layer of metal oxides such as MnO₂ [52], NiO [5], SnO₂ [53], Mn₃O₄ [54], and Co₃O₄ [5, 55]. A conversion reaction will happen at anode:



Where M stands for transition metals like Mn, Ni, Sn, Co and Fe [79].

Figure 1.1 shows the illustration of graphene/metal oxide composites. For example, Wu's paper reports that after being coated with Co₃O₄, their graphene-based 3D porous structure can

reach an outstanding specific capacitance (226 F/g), a high rate capability, and excellent cycling stability (no capacitance loss after 5000 cycles) [5].

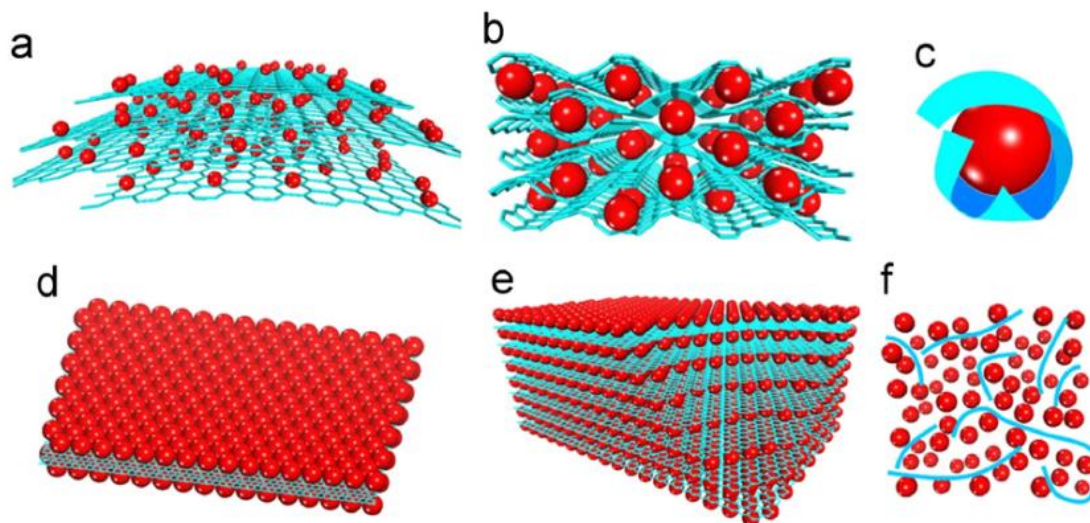


Figure 1.1, Schematic of structural models of graphene/metal oxide composites: (a) Anchored model: nanosized oxide particles are anchored on the surface of graphene. (b) Wrapped model: metal oxide particles are wrapped by graphene. (c) Encapsulated model: oxide particles are encapsulated by graphene. (d) Sandwich-like model: graphene serves as a template for the creation of a metal oxide/graphene/metal oxide sandwich-like structure. (e) Layered model: a structure composed of alternating layers of metal oxide nanoparticles and graphene. (f) Mixed model: graphene and metal oxide particles are mechanically mixed and graphene forms a conductive network among the metal oxide particles. Red: metal oxide particles; Blue: graphene sheets. [56]

1.2.3 3D porous graphene applications in ORR catalyst

In catalysis, 3D porous graphene can be highly efficient oxygen reduction reaction (ORR) catalyst after being functionalized. As a platform, 3D porous graphene can be doped with nitrogen (metal-free) to work as an ORR catalyst. Furthermore, N-doped graphene, together with metal nanoparticles (Fe, Co, etc. [57]) or metal oxides (Fe_2O_3 , Fe_3O_4 , etc. [58]), can also form a highly efficient catalyst for ORR.

As an example of a metal-free catalyst, Lai's paper constructs their catalyst on graphene obtained by assembling of graphene oxide into 3D structure and reduction [20]. Figure 1.2(a) shows their metal-free nitrogen-doped 3D graphene that were produced to be ORR catalysts. As

an example of nitrogen-doped graphene with metal oxides, Wu's paper reported that their 3D N-doped graphene with Fe_3O_4 nanoparticles shows better durability than the commercial Pt/C catalyst [58] as shown in Figure 1.2(b) But poor electrical conductivity of 3D graphene made from reduction of graphene oxide will suppress charge transport properties of catalysts. On the other hand, 3D graphene structure made from CVD growth of graphene have much better conductivity and provide a faster charge transfer rate for chemical reactions occurring at graphene/solution or graphene/gas interface than that made from graphene oxide, so it is promising to be used to produce better ORR catalyst in the future.

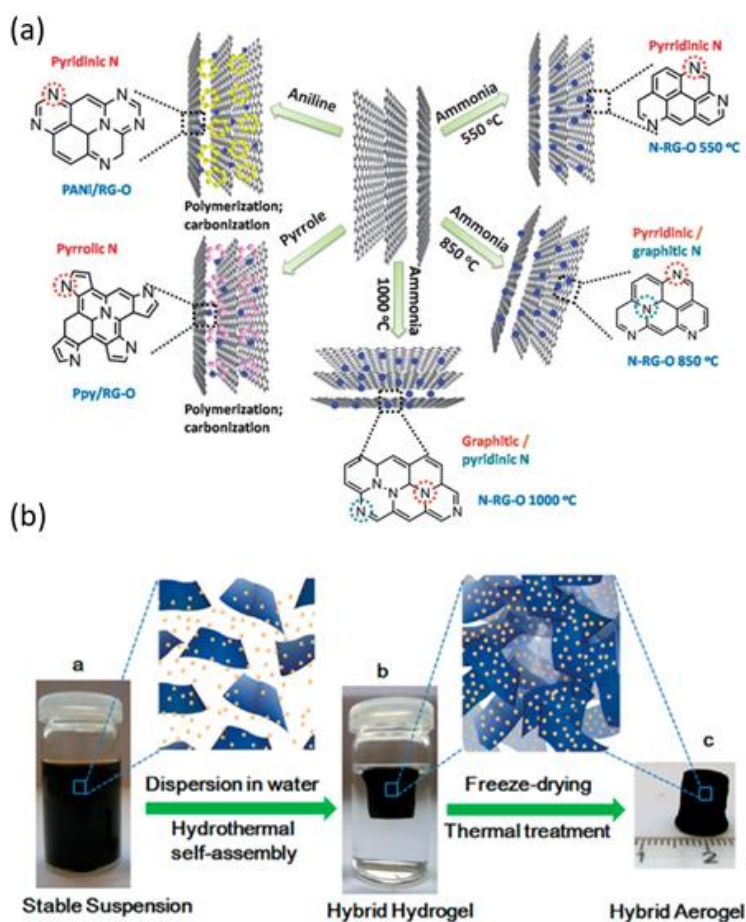


Figure 1.2, (a)Schematic diagram for preparation of nitrogen-doped graphene.[20] (b)Fabrication process for the 3D $\text{Fe}_3\text{O}_4/\text{N-GAs}$ catalyst.[58]

1.2.4 3D porous graphene applications in sensor probe

In sensor applications, 3D porous graphene can be used as a template for highly sensitive metal ion sensors and gas sensors [6, 59, 60]. The high electrical conductivity and large specific surface area of 3D graphene makes it a proper candidate for the sensitive heavy metal ion detection sensor: for example, the detection of lead ions and copper ions [6]. The high surface-to-volume ratio and potential catalytic properties of graphene makes it a proper candidate for gas-sensing applications, for example the detection of NO₂ and NH₃ [59, 60, 63].

As an example of gas-sensing, Wu's paper reported that their 3D graphene gas sensor synthesized from Ni films via CVD can detect NO₂ with high sensitivity [63] as shown in Figure 1.3(a–d). As an example of the heavy metal ion sensor, which is shown in Figure 1.3(e), they use graphene made from GO as their platform, and functionalize the graphene with bismuth to achieve a sensitive probe for heavy metal ion detection [6].

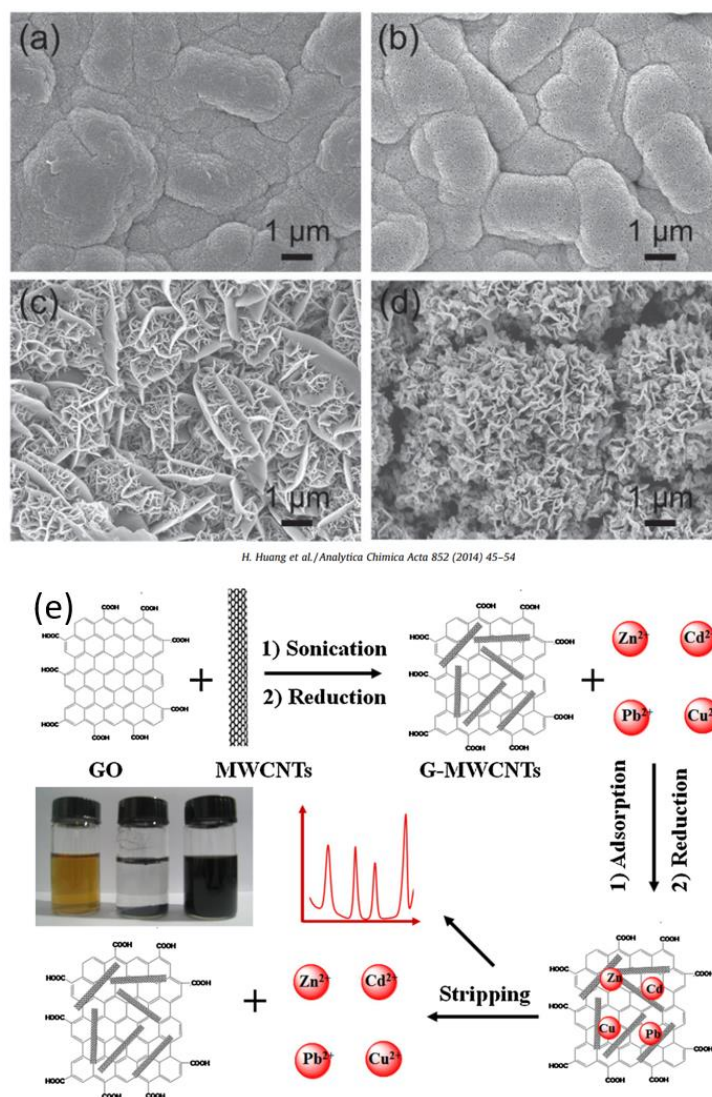


Figure 1.3 (a-d) SEM image of 3D graphene for gas sensing.[63] (e) Schematic diagram for the synthesis of 3D GO-MWCNTs hybrid nanomaterials on metal ions sensor [6].

1.2.5 Introduction of the 3D graphene manufacturing techniques

Different manufacturing techniques of graphene influence its mechanical and electronic properties [9, 21–25]. A predominant amount of work in the field has been focused on 3D graphene manufacturing techniques, aiming to produce graphene with high electrical conductivity and large specific surface area. There are two primary manufacturing techniques that have been widely used to produce 3D graphene—one is by the assembling and reduction of

graphene oxide (GO) and another is the CVD of graphene on 3D metal scaffolds [64], illustrated in Figure 1.4.

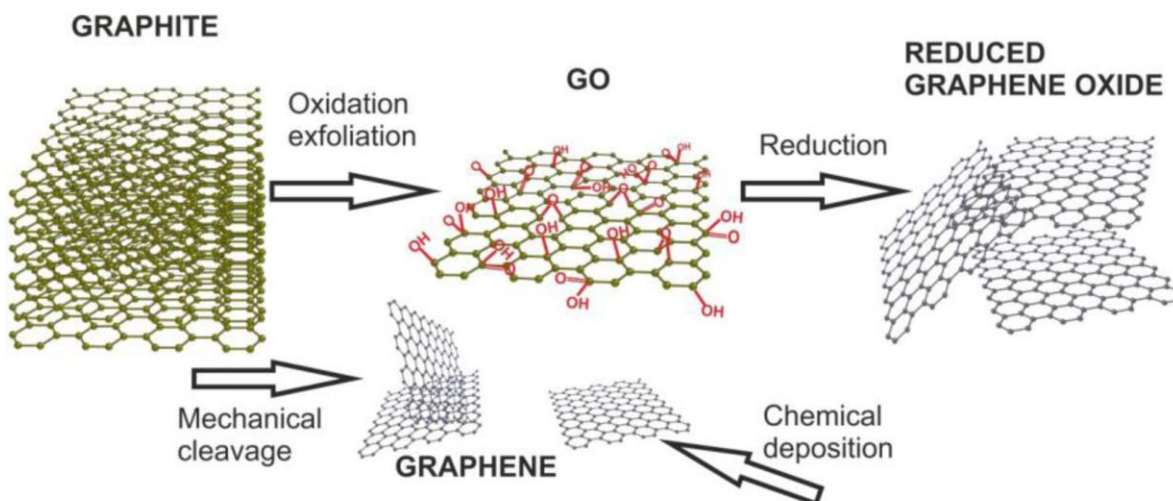


Figure 1.4, Two ways of approaching graphene. (Reduction of GO and CVD growth)[64].

People initially use graphite oxide (GO) dispersed in polymer to construct 3D graphene. GO dispersion and self-assembling is the relatively easier method of synthesis and scale-up for commercial or industrial use but with limited performance in conductivity [21, 22]. Another technique is chemical vapor deposition (CVD) that is conducted on 3D metal scaffolds to reach graphene that has the same structure with the parent metal precursor [9, 23, 24, 25]. As a template-based method, CVD enables precise and facile control over the pore architecture.

1.2.5.1 Assembling and reduction of graphene oxide (GO)

GO dispersions can self-assemble into highly porous and light-weight sponges through hydrothermal or chemical methods; subsequently, a reduction under the forming gas can be conducted to form GO-based graphene [61, 62]. This technique has been widely used in producing graphene with 3D structure [21, 22]. However, graphene from GO assembly and reduction will unavoidably have limitations with respect to conductivity, defect density and 3D

structure control, due to high inter-sheet junction contact resistance, insufficient reduction of GO and difficulties in controlling the GO dispersion [21, 22].

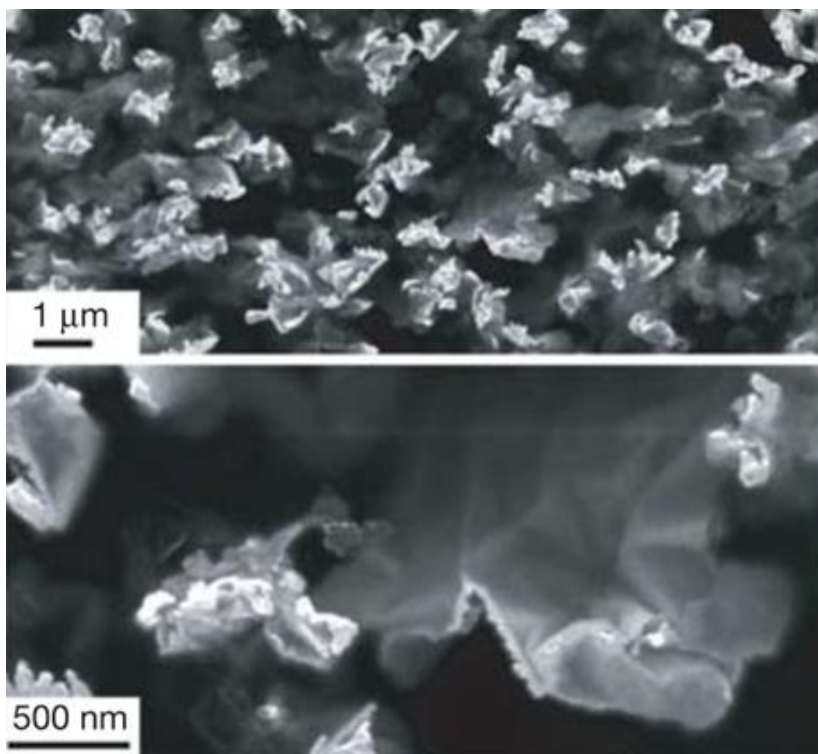


Figure 1.5, Low and high magnification SEM images from a fracture surface of composite samples of 0.48 vol.% graphene in polystyrene.[21]

For example, Sasha's paper uses polymer as its template [21] and disperses GO into polymer to form a 3D structure. Following this, a reduction is conducted to improve the electric properties, as shown in Figure 1.5. In Ramanathan's paper, their functional graphene sheets (FGS) are produced from graphite oxide with the use of poly(methacrylate) (PMMA) and FGS in combination [22]. Though the conductivity is improved after the reduction of graphite oxide, their graphene is still not a proper material for electrical applications. Additionally, 3D structures from GO are also hard to be designed into particular shapes because it is hard to control the dispersion of GO [21, 22].

1.2.5.2 Chemical vapor deposition (CVD) growth on metal template

CVD has been an important method in producing graphene since it was reported and identified in 2004 [24-25, 88]. In general, graphene from CVD growth preserves higher crystalline quality and enhanced electrical and mechanical properties in comparison to graphene made from GO assembling and reduction [9, 24–26]. Several reports focus on manufacturing graphene via CVD of methane or ethylene gases as precursors on Cu, Ni or Cu-Ni alloy substrates in 2D films [23]. In the case of 3D structure, however, Ni is the main scaffold material used to produce graphene despite the problems in controlling thickness and uniformity [25, 33, 67].

CVD growth of graphene can be explained in the following steps: the heating step, where the metal scaffolds and gases are heated to the pre-process temperature; the annealing step, where the temperature is maintained under the forming gas (hydrogen and argon) to reduce the catalyst surface; the growing step, where the carbon source such as CH_4 is introduced, the decomposition, adsorption and diffusion of carbon source happens over the catalyst substrate, leads to the growth of graphene; the cooling step, where the furnace is cooled down to room temperature under the environment of the forming gas [67]. An illustration of the growing step is provided in Figure 1.6 to elaborate on this step further, where the related chemical reactions occur and graphene grows [67].

Two kinds of growth kinetics are observed in the CVD of graphene [67]. One is observed on Cu scaffolds, where the graphene grown over the metal substrates will reduce the catalytic activity due to catalyst poisoning. Overall process is when the reaction is promoted on the surface (adsorption, decomposition, and diffusion of molecules), monolayer graphene is preferentially grown [10, 67]. Another growth kinetic is observed on Ni and other common transition metals scaffolds (Co, Ru, etc.), where the CVD growth of graphene occurs due to

decomposition of precursor gas, carbon adsorption and bulk diffusion of carbon at high temperatures and surface segregation during cool down, and tends to grow thicker graphene layers; this is due to the high solubility of carbon [25, 33, 67]. The two kinetics are illustrated in Figure 1.7.

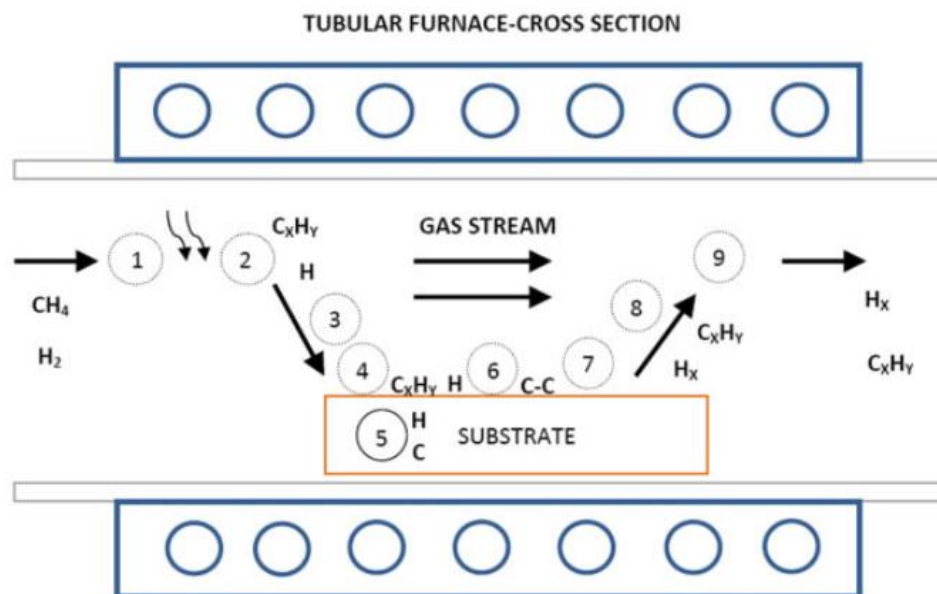


Figure 1.6, Schematic diagrams of thermal CVD processes in the case of graphene from CH_4/H_2 mixtures. 1.Transport of reactants by forced convection. 2.Thermal activation. 3.Transport of reactants by gas diffusion from the main gas stream through the boundary layer. 4. Adsorption of reactants on the substrate surface. 5. Dissolution and bulk diffusion of species depending on the solubility and physical properties of the substrate. 6. Growth of the film. 7. Desorption of by-products from the surface. 8. Transport of by-products by diffusion through the boundary layer and back to the main gas stream. 9. Transport of by-products by forced convection away from the deposition region.[67]

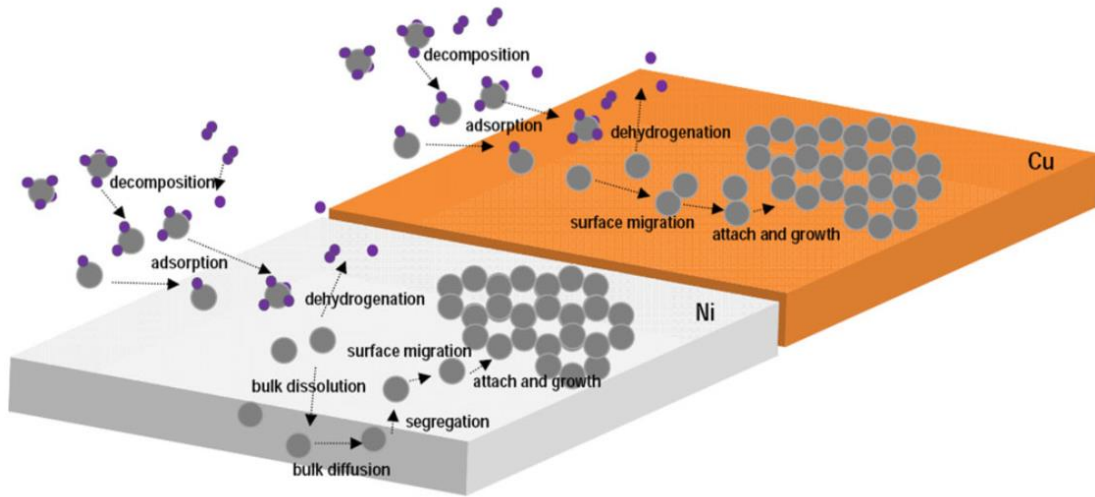


Figure 1.7 Growth kinetics in CVD-produced graphene on various catalyst: Case of CH₄ on Ni and Cu. [67]

1.2.6 Graphene layers thickness control and graphene stacking mode on 3D porous graphene

As mentioned in 1.2.1, the differences in graphene thickness and graphene stacking modes have huge influence on the electrical [10, 27, 43, 43] and mechanical properties of graphene [51].

The problem with graphene thickness controlling can be resolved by using Cu-Ni alloy scaffolds in CVD graphene growth; however, as mentioned before, works are always limited to 2D films [27]. Transition metals such as Cu and Ni are widely used in the CVD growth of graphene, and it is much easier to uniformly grow few layers graphene on the Cu template via CVD [28, 61, 74]; the huge difference of carbon solubility between Cu (<0.001 atomic%) and Ni (>0.1 atomic%) is one primary reason for the difference [10]. The use of Cu-Ni alloy provides a way to control the carbon solubility of the metal template by changing the fraction of Ni in Cu. For example, in Takesaki's paper, Cu-Ni alloy is used to control the CVD graphene; they, as shown in Figure 1.8 [74], grow uniform graphene over the 2D Cu-Ni alloy films. The control of

graphene layers' thickness is difficult to achieve in the 3D porous graphene, primarily because it is difficult to achieve 3D porous Cu-Ni alloy scaffolds. Inspired by the concept of using 2D Cu-Ni alloy films in CVD, the method of producing 3D porous Cu-Ni alloy scaffolds is studied in this thesis.

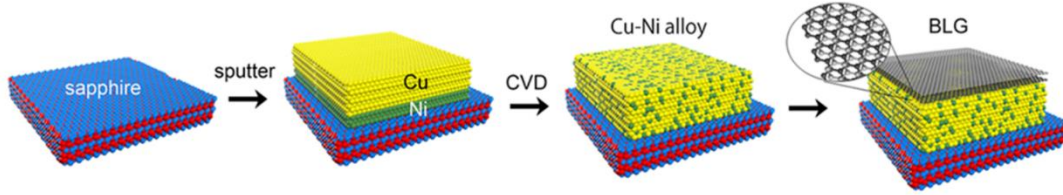


Figure 1.8, Schematics of the CVD growth of uniform graphene over a Cu-Ni alloy film.[74]

The layers stacking mode on 3D porous graphene is complicated, and there can be multiple-layers graphene with Bernal stacking and turbostratic stacking features [45].

Multiple-layers graphene (MLG) shown on 3D graphene can be classified into Bernal stacking graphene and turbostratic graphene [42–44]. Bernal stacking graphene is shown in Figure 1.9(a), where half of the atoms lie over the center of a hexagon in the lower graphene sheet and half of atoms lie over an atom, the electronic properties are suppressed due to the lowest energy configuration of the stacked graphene layers; this implies that the interlayer coupling between the adjacent carbon layers changes the dispersion of the electronic states and opens a band-gap, thereby suppressing the electronic properties [44]. Turbostratic graphene is shown in Figure 1.9(b) and is the multiple-layers graphene with relative rotations of more than 20° between Bernal stacking, and effectively decouple the electronic states of the adjacent layers, preserving properties similar to that of single-layer graphene (SLG) [45]. SLG is a two-dimensional network of sp^2 bonded carbon atoms that has exhibited remarkable electronic properties [42, 43]. However, in the case of the actual applications of 3D graphene, SLG is not

an option because of the following reasons. First, the mechanical properties of 3D graphene decrease with density, a large-scale 3D structure with only SLG is fragile, lost its advantage over most polymeric cellular materials and hard to be applied in real applications [51]. Second, interfacial interactions between graphene and its substrate will drastically alter the electronic structure; furthermore, it is hard to manufacture porous 3D structure with SLG. Even if SLG on 3D structure is realized in the future, metal scaffolds need to be etched off to exclude the interfacial interactions between metal and graphene. However, if the etching is conducted, the two layers of SLG grown from both surface of metal will then tend to stack into a two-layers graphene [42–44].

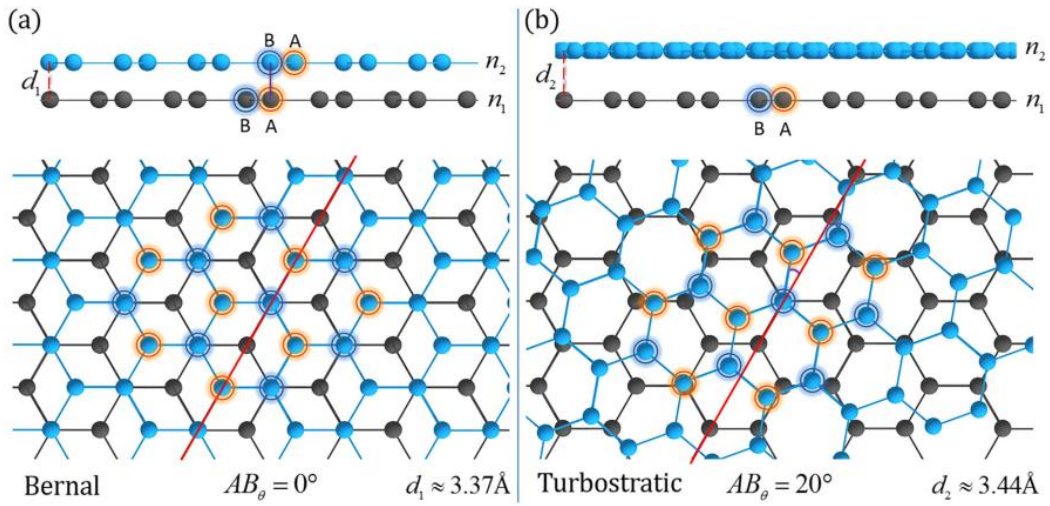


Figure 1.9, illustration of (a) Bernal stacking graphene and (b) Turbostratic stacking graphene [42].

Considering the electronic properties of graphene, both SLG and turbostratic graphene can meet the requirements for electrical applications [42–45]; however, if the manufacturing limitations and mechanical requirements are taken into consideration [51], turbostratic graphene is a better choice for 3D porous graphene.

Chapter 2

Synthesis of bicontinuous Cu-Ni alloy scaffold

2.1 Motivation and background

The goal is to produce a bicontinuous Cu-Ni alloy 3D architecture (bi-CuNi) for use as a metal scaffold for CVD graphene growth. In order to produce the desired 3D architectures, bicontinuous interfacially jammed emulsion gel (bijel) is used as polymer template for electroless deposition of Ni and Cu to form the bi-CuNi alloy in a bicontinuous morphology.

We use bijel templates to improve upon prior work where commercially produced sponge-like porous metal scaffolds have been widely used in CVD growth. However, these have limited control over pore (100 μm) and ligament size distribution compared to metal scaffolds made from bijel templates [14-16]. On the other hand, bicontinuous porous morphology of the metal scaffolds investigated here inherited from the bijel template presents a unique and pertinent paradigm in which both the solid and void phases form a convoluted percolating path throughout the sample volume; each phase exists as a continuous phase, and it is easy to traverse to any point within one phase without crossing the phase boundary, thereby providing advanced transport, mechanical and electrochemical properties [17–19]. In terms of applications, the bicontinuous structure benefits performance in fuel cell systems, where electrochemical reactions

are involved and bicontinuous electrode can help with the gas and charge transport [29-31].

Illustration of the bicontinuous structure provided from bijel templates is provided in Figure 2.1.

With the preservation of bicontinuous morphology and large specific surface area of bijel [17–19], bi-CuNi scaffolds can be used to control CVD graphene growth [28, 61] and produce 3D graphene with large specific surface area and bicontinuous structure.

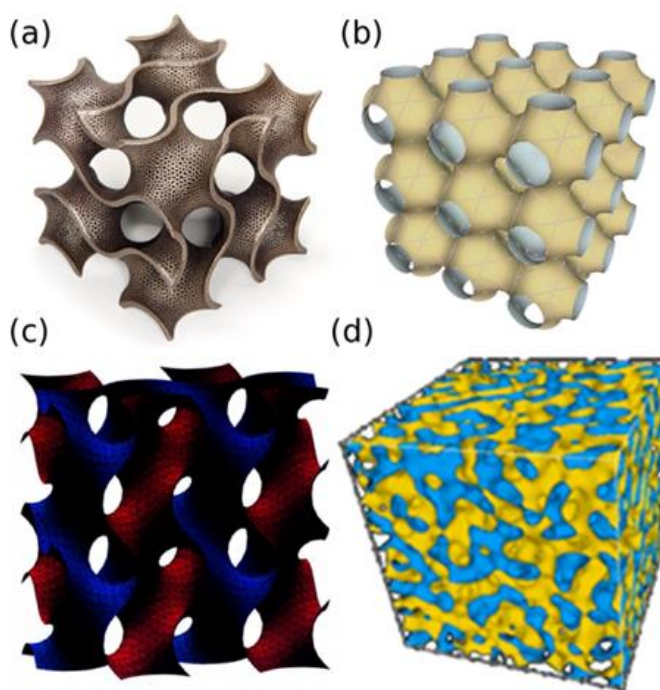


Figure 2.1, Examples of ideal bicontinuous structure [17]. (a) Schoen's gyroid (b) Schwarz P-surface (c) bicontinuous cubic structure (d) spinodal decomposition.

2.2 Experimental Design

The experiment method of bi-CuNi scaffold synthesis is described in this section. First, the bijel template is made from spinodal decomposition, then biNi scaffold is made from the electroless deposition of Ni on bijel template surface, after etching is conducted on biNi followed

by a electroless deposition of Cu to form bi-CuNi scaffold. The bi-CuNi scaffold is ready to be used to grow graphene via CVD process. From prior work it is known that it is difficult to uniformly distribute Cu atoms on the inside of the etched biNi structure, it has been observed that the electro-deposition of Cu on biNi always ends up with the coating only on the outside of the structure; the replacement reaction between Cu ions and metallic Ni can't ensure enough amount of Cu on the surface of biNi. However, considering the high solubility of CuSO₄ solution at high temperature and the uniform distribution of Cu ions in CuSO₄ solution, it provides a way to uniformly distribute Cu atoms inside the porous structure by filling the biNi scaffolds with CuSO₄ solution.

2.2.1 bijel templates synthesis

Poly (ethylene glycol) diacrylate bijel-based scaffolds (bi-PEGDA) is used as the bijel template [17]. The bi-PEGDA templates are formed by first dispersing the dried silica particles in ultrapure water using a sonic probe (Branson Sonifer 250). Typical volume fractions of silica range from 0.005-0.06. An appropriate amount of 2,6-lutidine is then added to give a near-critical composition and the suspension is briefly agitated using a vortex mixer. 200 μ L of the single-phase suspension is transferred to cylindrical microscopy vials of 5 mm inner diameter and irradiated in a microwave oven at 120 W for 50 s, then immediately irradiated again for 70 s at 50W. Sample is quickly transferred to an incubator maintained at 60 $^{\circ}$ C, and left unperturbed for at least 15 min. A small amount (typically 30–40 μ L per 200 μ L suspension) of hydrophobic monomer and photoinitiator (1% v/v, Darocur 1173, Ciba) is placed in contact with the bijel. In this case, bijel is polymerized using bi-PEGDA monomer. Sample is made by filling rectangular capillaries (Vitrocom, Mountain Lakes, NJ) with the single-phase suspension and placing the capillaries on an aluminum block preheated to 60 $^{\circ}$ C and introducing the monomer through the

sides of the capillary. The containers were sealed and allowed to equilibrate undisturbed for at least 4 h. While samples were still warm, photopolymerization was carried out using a UV lamp (Omnicure 1000).

2.2.2 bi-CuNi synthesis

2.2.2.1 Electroless deposition of Ni

Electroless deposition is used to deposit Ni on PEGDA templates synthesis to coat a thin layer with thickness (in the order of microns) of metal on the surface of the bijel template. In order to ensure Ni deposition on the template, an activation of surface is conducted first by using palladium chloride (Sigma Aldrich, St. Louis, MO, CAS # 7647-10-1) solution. The polymerized bijel template is soaked in a saturated solution of palladium chloride in anhydrous ethanol overnight, washed by isopropyl alcohol (IPA) before electroless deposition.

Subsequently, electroless nickel deposition is performed in a bath with 0.02M nickel chloride hexahydrate (Fisher Scientific, Hampton, NH, CAS # 7791-20-0), 0.02M sodium tartrate dehydrate (Aldrich Chemical Company, Milwaukee, WI, CAS # 6106-24-7), 1M hydrazine (Sigma-Aldrich, St. Louis, MO, CAS # 10217-52-4), and 1 vol% 1-Propanol (Fisher Chemical, Waltham, MA, CAS # 71-23-8) at a temperature of 95°C and PH of 10, for 330 min. Following this, the sample is washed by IPA. After electroless deposition of Ni, the scaffold is heat-treated under 1 hour at 300°C and 1 hour at 500°C to decompose the residual polymer template, followed by 8 hours' reduction at 450°C under the forming gas (5% hydrogen, 95% argon) to reduce the oxidized Ni to the metallic state.

2.2.2.1 Electrolesss Deposition of Cu

Before the electroless deposition of Cu on biNi, to help preserve the porous morphology the bi-Ni scaffold is partially etched to widen the pores. Etching helps to reduce the thickness of

Ni, and it is a necessary step for maintaining a bi-continuous porous morphology. The etching is conducted by 1M HCl for 5 minutes under sufficient sonication. The sonication is used to accelerate the diffusion of HCl, in order to ensure that the dissolving of the biNi is uniform in the biNi surface. To ensure that the etching reaction will end at the same time on the biNi surface, NaOH is used to neutralize the HCl to stop etching, which is also under sonication. Figure 2.2 shows the SEM image of biNi after etching, and the bijel morphology is well preserved. Figure 2.3 shows the same biNi sample before and after the etching. The sample floats up after etching, indicating the loss of Ni.

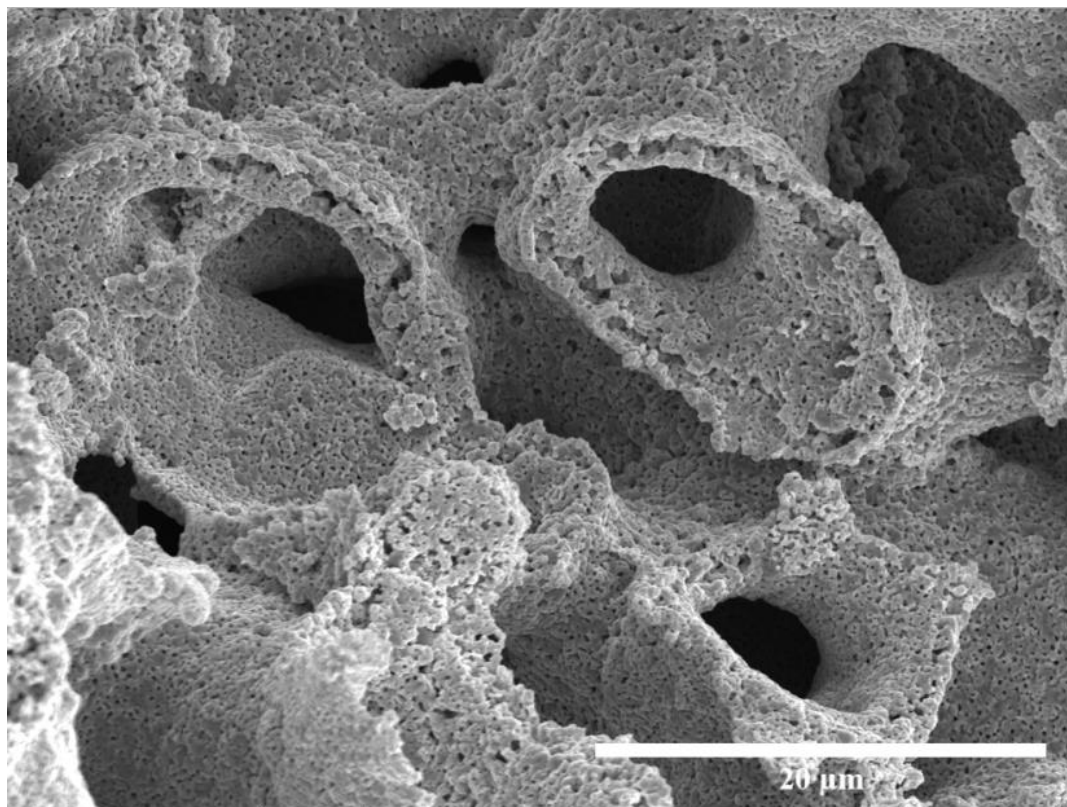


Figure 2.2, SEM image of etched biNi.

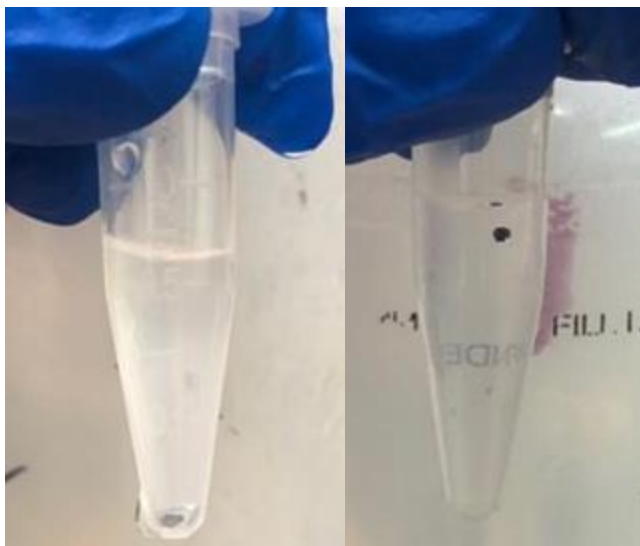


Figure 2.3, biNi before and after been etched with 1M HCl for 5 min under sonication.

2.2.2.2 Electroless Cu deposition

After the etching of biNi, the electroless Cu deposition is done on the etched biNi to form bi-CuNi. Electroless deposition of Cu is defined in 4 steps: (a) distribution of saturated CuSO_4 into the biNi porous structure, (b) drying on a hotplate, (c) decomposition of crystal CuSO_4 and (d) formation of the Cu-Ni alloy. The steps (a-d) together is called one cycle of electroless Cu deposition, and the sample made from it is called one cycle bi-CuNi.

Figure 2.4 shows the illustration of electroless Cu deposition. In step (a), the biNi template is soaked in the saturated CuSO_4 (Sigma Aldrich, St. Louis, MO, CAS #7758-99-8) solution with a 80 °C water bath to have an 81g/100 ml solubility of CuSO_4 in DI water. Following this, a 20 mins sonication is followed under the same water bath to fill the biNi with a CuSO_4 solution. In step (b), the sample is dried on the hotplate for 12 hours at 80 °C, under the air, to form water-free CuSO_4 crystals. In the experiment, when the color of CuSO_4 crystals turns from blue to white, it is considered that there is no water left. In step(c), the sample is heated to 950 °C under the air for 1 hour, and in this step, the CuSO_4 crystals will decompose

and form CuO. In the step (d), the sample is loaded into a 1'' quartz tube at a pressure of approximately 10^{-2} torr while flowing forming gas (5% hydrogen, 95% argon) at 100 SCCM for 1 hour at 450 °C. Thus, the CuO is reduced to Cu.

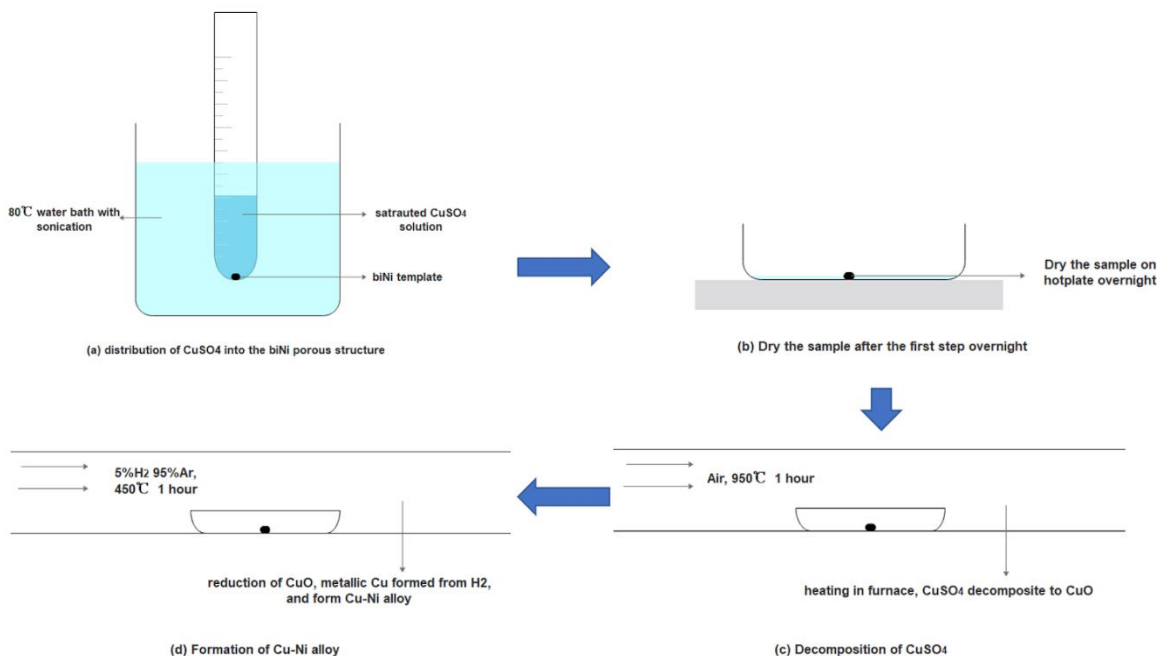


Figure 2.4, Illustration of the four steps for one cycle of electroless Cu deposition.

Scanning electron microscopy (SEM) is used to image the sample's surface morphology. The biNi is deposited with Cu, using the experiment method in Figure 2.4 for one cycle to form bi-CuNi from etched biNi and biNi respectively. Figure 2.5 shows the SEM images of bi-CuNi made from biNi without etching and with etching respectively. It is easy to ascertain that bi-CuNi from biNi, without etching, lost its bijel morphology.

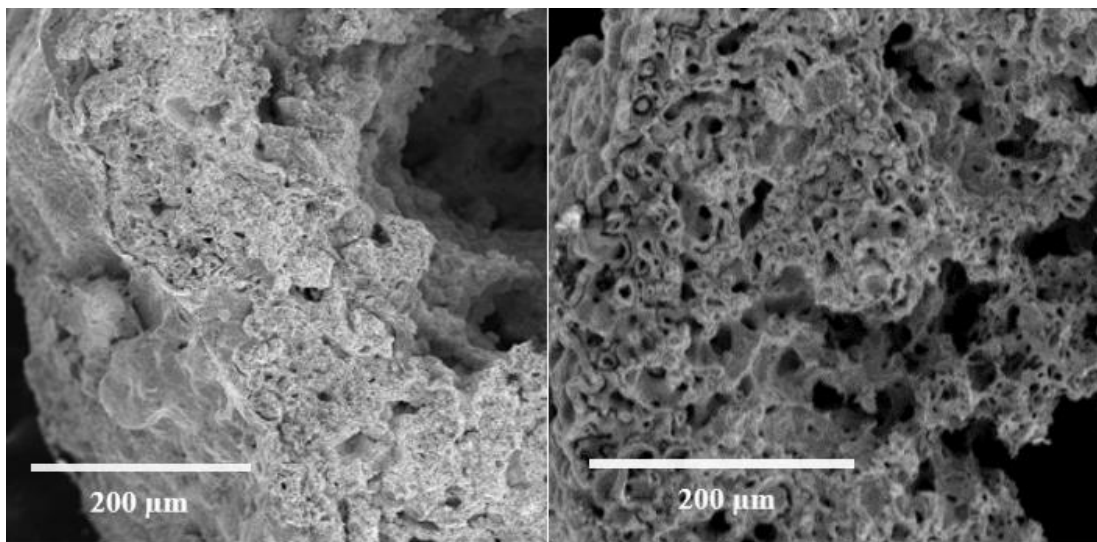


Figure 2.5, SEM of bi-CuNi and biNi. On the left is a bi-CuNi alloy template growing from biNi without etching. The picture on the right shows the morphology of biNi.

2.2.3 Estimate of Cu layer thickness

An estimate of the thickness of Cu deposited on the surface of biNi scaffolds by one cycle of electroless Cu deposition under different electroless deposition temperature and pore size was calculated. As shown in Figure 2.6, on the left is a cylindrical tube used to model a pore in the biNi template, which will be filled with saturated CuSO_4 solution in the biNi template. On the right is the tube after all the Cu ions in the solution have been reduced to metallic Cu. There are two assumptions in the calculation. The first assumption is the conservation of Cu atoms within the tube model, which means that the number of Cu atoms inside the tube model will not change during the electroless Cu deposition. The second assumption is that all the Cu ions in the solution will turn to metallic Cu and deposit to the inner face of the biNi pore model. In this calculation, an ideal situation is used where a uniform Cu layer is achieved, to show average layer thickness.

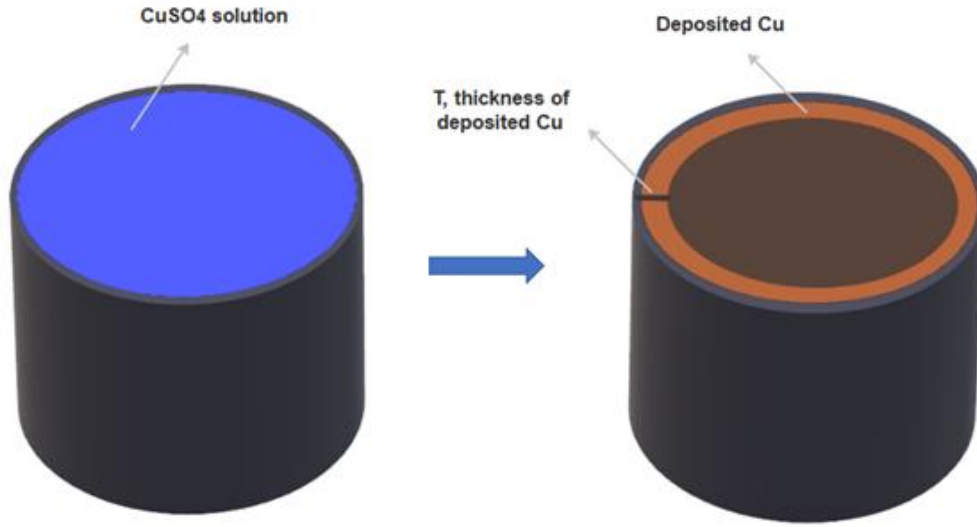


Figure 2.6, Diagram of Cu electroless deposition in a cylindrical tube model.

The diameter of the pore is defined as D (μm), the height of the tube model is defined L (μm), the solubility of CuSO_4 as C ($\text{g}/100\text{ml}$), the density of saturated CuSO_4 solution is defined as ρ (g/cm^3), the thickness of the deposited Cu on the Ni surface is defined as T (nm), the density of the metal Cu is defined as ρ' ($8.96\text{g}/\text{cm}^3$), and the relative mass of Cu and CuSO_4 are defined as M_{Cu} and M_{CuSO_4} . According to the conservation of Cu atoms between CuSO_4 solution and metallic Cu within the tube model, the volume of the metallic Cu inside the tube model can be calculated:

$$V = \left(\frac{\pi D^2}{4} \right) \times L \times \rho \times \frac{C}{C+100} \times \frac{M_{\text{Cu}}}{M_{\text{CuSO}_4}} \div \rho' \quad \text{equation (1)}$$

Assume that the diameter of the pore after having been deposited with Cu is D' :

$$D' = D - 2T \quad \text{equation (2)}$$

The volume between the cylinder with diameter D and the cylinder with diameter D' is V, which stands for the metallic Cu volume, as shown in Figure 2.6. Therefore, V can also be expressed by D and D':

$$V = \left(\frac{\pi D^2}{4} \right) - \left(\frac{\pi D'^2}{4} \right) \quad \text{equation (3)}$$

Combine equation (1), (2) and (3):

$$T = D \left(\frac{1 - \sqrt{1 - 2 \frac{\rho C}{5 \rho'}}}{2} \right) \quad \text{equation (4)}$$

T (nm) is the thickness of the deposited Cu, D (μm) is the diameter of the pore, C (g/100ml) is the solubility of CuSO₄ and ρ is the density of CuSO₄ solution at solubility C, and ρ' (8.96g/cm³) is constant, and stands for the density of metallic Cu. The table 2.1 presents the relationship between the temperature, solubility C and density ρ. The data is gained from experiments.

Table 2.1, Relationship between the temperature, CuSO₄ solubility and CuSO₄ solution density.

Temperature (°C)	solubility C (g/100ml)	density ρ (g/cm ³)
80°C	81 g/100ml	1.72 g/cm ³

60°C	61.8 g/100ml	1.57 g/cm ³
40°C	43.6 g/100ml	1.39 g/cm ³

The relationships between the Cu thickness, pore size and temperature are estimated from the above described calculation. Results are shown in Figure 2.7. The deposited Cu layer thickness increases with the increase of the pore diameter by a linear relationship, and also increases with the increase of the Cu electroless deposition temperature.

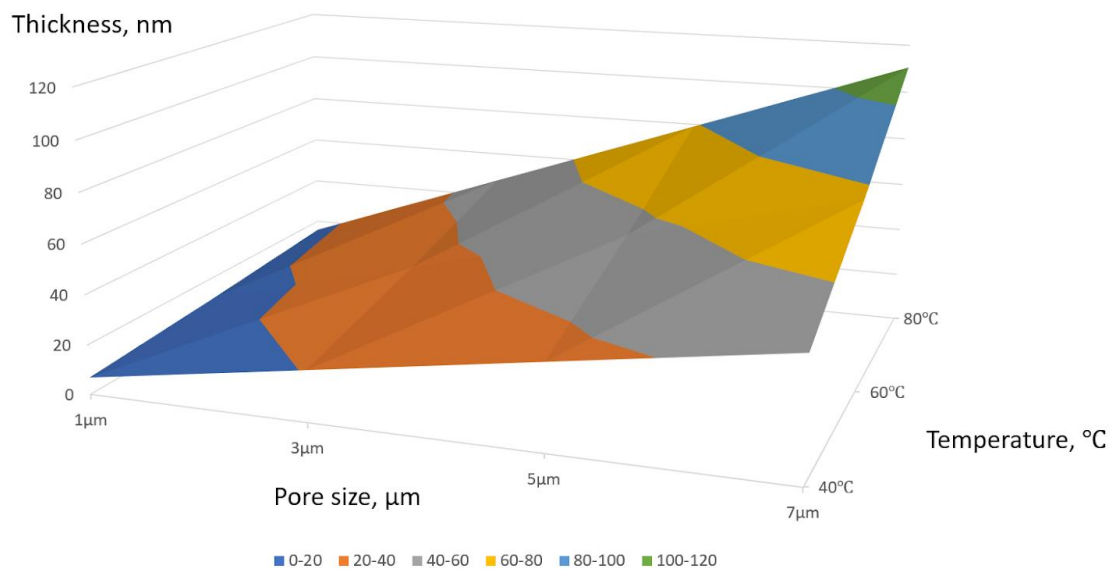


Figure 2.7, Relationship between the hole size (μm), electroless Cu deposition temperature (°C) and the deposited Cu thickness (nm).

2.3 Characterization

Scanning electron microscope (SEM) and energy dispersion spectrum (EDS) analysis are used to verify the surface morphology and Cu concentration of prepared bi-CuNi. The Cu concentration is calculated by using the data from EDS analysis on the bi-CuNi cross section, with the following calculation: $C_{Cu} = (W_{Cu}) / (W_{Cu} + W_{Ni})$, where C_{Cu} stands for Cu concentration in the bi-CuNi scaffold, W_{Cu} stands for the weight of Cu in the cross section, and W_{Ni} stands for the weight of Ni in the cross section. Figure 2.8 (a-c) are SEM and EDS images of bi-CuNi cross section with 2 cycles of electroless Cu deposition, from which a Cu concentration of 46.8% is calculated; Figure 2.8 (d-f) are SEM and EDS images of bi-CuNi cross section with 1 cycle of electroless Cu deposition, from which a Cu concentration of 35.8% is calculated.

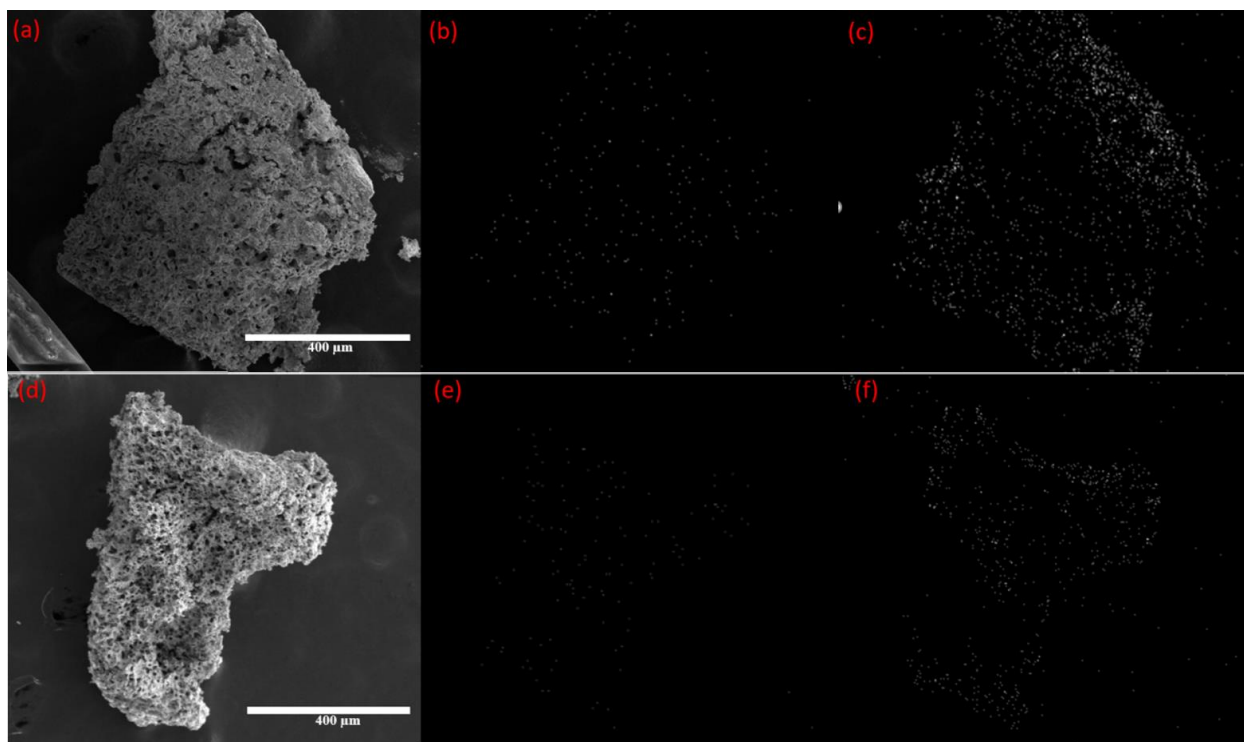


Figure 2.8, (a-c) SEM and EDS images of bi-CuNi cross section of 2 cycles bi-CuNi, (a) SEM image, (b) EDS Ni map and (c) EDS Cu map. (d-f) SEM and EDS images of bi-CuNi cross section of 1 cycles bi-CuNi, (d) SEM image, (e) EDS Ni map and (f) EDS Cu map. Scale bar is 400μm.

Figure 2.9 shows the morphology of the two samples above by SEM images. Figure 2.9 (a) shows the SEM image of 46.8 weight% Cu-Ni alloy, the porous morphology is well kept. Figure 2.9(b) shows the SEM image of 35.8% weight of the Cu-Ni alloy. The morphology is maintained better than that of Figure 2.9(a).

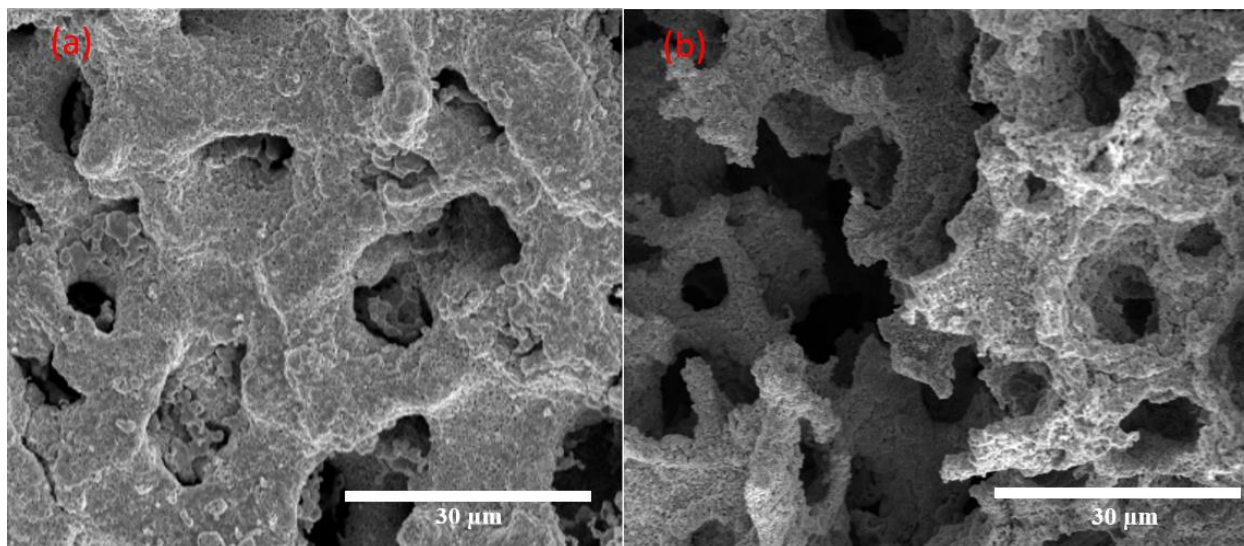


Figure 2.9, SEM image on different metal scaffolds. (a) SEM image of the 2 cycles bi-CuNi template, 46.8 weight% Cu in the bi-CuNi template. (b) SEM image of the 1 cycle bi-CuNi template, 35.8 weight% Cu in the bi-CuNi template.

2.4 Conclusion

In this chapter, different concentrations of Cu in the bi-CuNi scaffolds are achieved through varying the number of electroless deposition cycles of Cu on a bi-Ni scaffold. One cycle and two cycles of electroless deposition are conducted to produce bi-CuNi that have a Cu concentration of 35.8% and 46.8%, respectively. The porous morphology is preserved in both the samples, shown by Figure 2.9. The calculation shown in Figure 2.7, which indicates the thickness of the Cu layer deposited on bi-Ni offers the possibility of achieving a more precise Cu concentration control in bi-CuNi. However, further research is required to be done to find proper Cu electroless deposition conditions such as temperature and the number of deposition cycles.

Chapter 3

CVD graphene growth on bi-CuNi

3.1 Motivation and background

The overall goal is to achieve a 3D architecture composed of bicontinuous 3D graphene with turbostratic stacking of the layers. Turbostratic graphene is comprised of multiple graphene layers with interlayer rotations that alleviate orbital hybridization resulting in carrier mobilities similar to that of SLG, which could enable the ballistic transport of electrons through decoupled graphene layers [42]. High mobility of charge carriers has attracted considerable interest in high-speed electronics, so turbostratic graphene is promising for future electronic applications such as integrated circuits [81-83].

As mentioned before, in 2D films, the number of layers of the graphenes have been controlled by the use of the Cu-Ni alloy in chemical vapor deposition (CVD)[27,28]. In the present study, control of the 3D graphene growth is achieved through the use of bicontinuous Cu-Ni alloy scaffolds (bi-CuNi). The stacking mode can be analyzed by the Raman spectra[42–44]. The graphene stacking mode is analyzed by 2D intensity full width at half maximum (I_{2D} FWHM), 2D intensity (I_{2D}), and 2D /G intensity ratio (I_{2D} / I_G) of the Raman spectra. The Raman spectra probes the electronic and vibrational properties of molecules and crystalline materials

through the inelastic scattering of photons by phonons and is a powerful tool for graphene characterization[68]. The stacking mode of multiple-layers of graphene including the turbostratic graphene and the Bernal stacking graphene can be analyzed by the Raman spectra, and the features of the Raman 2D mode is always employed as signatures of the turbostratic graphene[42,68]. The Turbostratic graphene is multi-layered graphene with relative rotations between carbon layers and can effectively decouple the electronic states of the adjacent layers, preserving excellent electronic properties similar to that of SLG.[45] However, Bernal stacking is widely observed in the CVD graphene[42-44,69], in which the inter-layer coupling between adjacent carbon layers will change the dispersion of electronic states and open a band-gap, and end up suppressing the electronic properties[44]. Therefore, it is important to know what kind of graphene stacking mode is in the 3D graphene from bicontinuous Cu-Ni alloy scaffolds (bi-CuNi-3DG).

In the Raman spectra, the 2D intensity full width at half maximum (I_{2D} FWHM) is different between the Bernal stacking graphene layers and the turbostratic graphene[70,71]. In a region of multiple-layered graphene, a I_{2D} FWHM on the order of 30cm^{-1} indicates a turbostratic graphene feature and the preservation of the SLG electronic structure[42]. As shown in Figure 3.5, in different growth conditions, a I_{2D} FWHM can be as low as 27cm^{-1} in the turbostratic graphene, and a I_{2D} FWHM around 100cm^{-1} can be considered as the Bernal stacking graphene. Also, high I_{2D} values suggest the absence of Bernal stacking, supporting the presence of a turbostratic graphene, due to the decoupled nature of a turbostratic graphene[42,73].

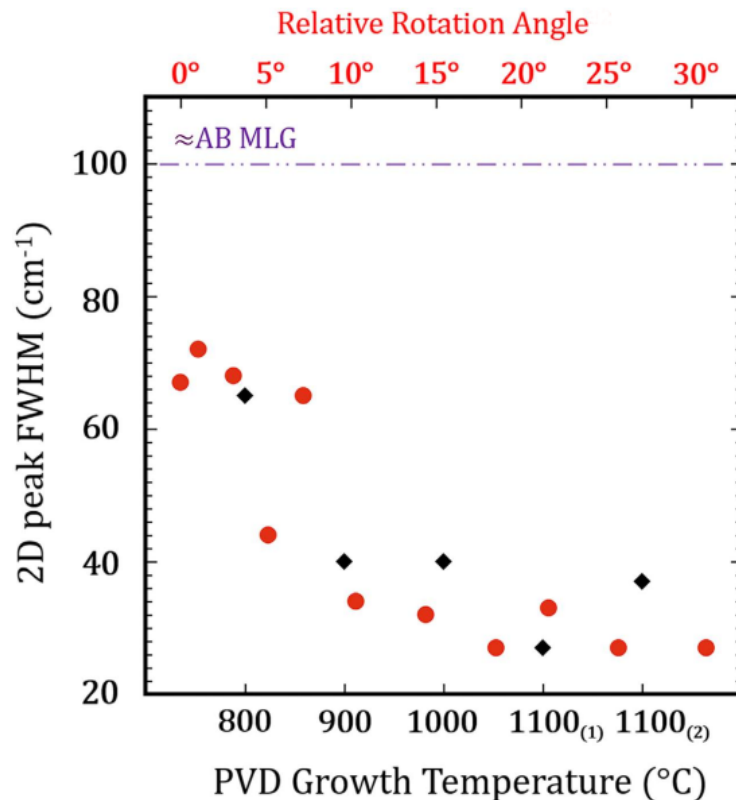


Figure 3.1, The relationship between I_{2D} FWHM and turbostratic graphene, with different relative rotation angle. The red points are from Kim's paper [72], the black points from Garlow's paper [42]. The purple line indicates the I_{2D} FWHM for the Bernal stacking graphene [42].

3.2 Experimental Design

The CVD of the graphene is conducted on etched biNi template and bi-CuNi scaffolds with a Cu weight concentration of 46.8% and 35.8%. All samples were loaded into a 1" quartz tube and evacuated to a pressure of approximately 10^{-2} torr while flowing forming gas (5% H₂ in Ar) at 100 SCCM into the system. The furnace is purged under vacuum/forming gas for 1 hour at ambient temperature, followed by a ramp to 954°C, at a rate of 30 °C/min. The samples are held at 954 °C for 25 minutes for one anneal, following which the temperature decreases to 950 °C at a rate of 10 °C/minute and is held for another hour for another anneal. At this point, 5 SCCM

CH₄ in the 100 SCCM forming gas is introduced into the system for 5 minutes. Subsequently, the CH₄ is turned off and the furnace is actively cooled from 950 °C to 250 °C at 15 °C/s under forming gas, with natural cooling to room temperature.

3.2.1 SEM data discussion

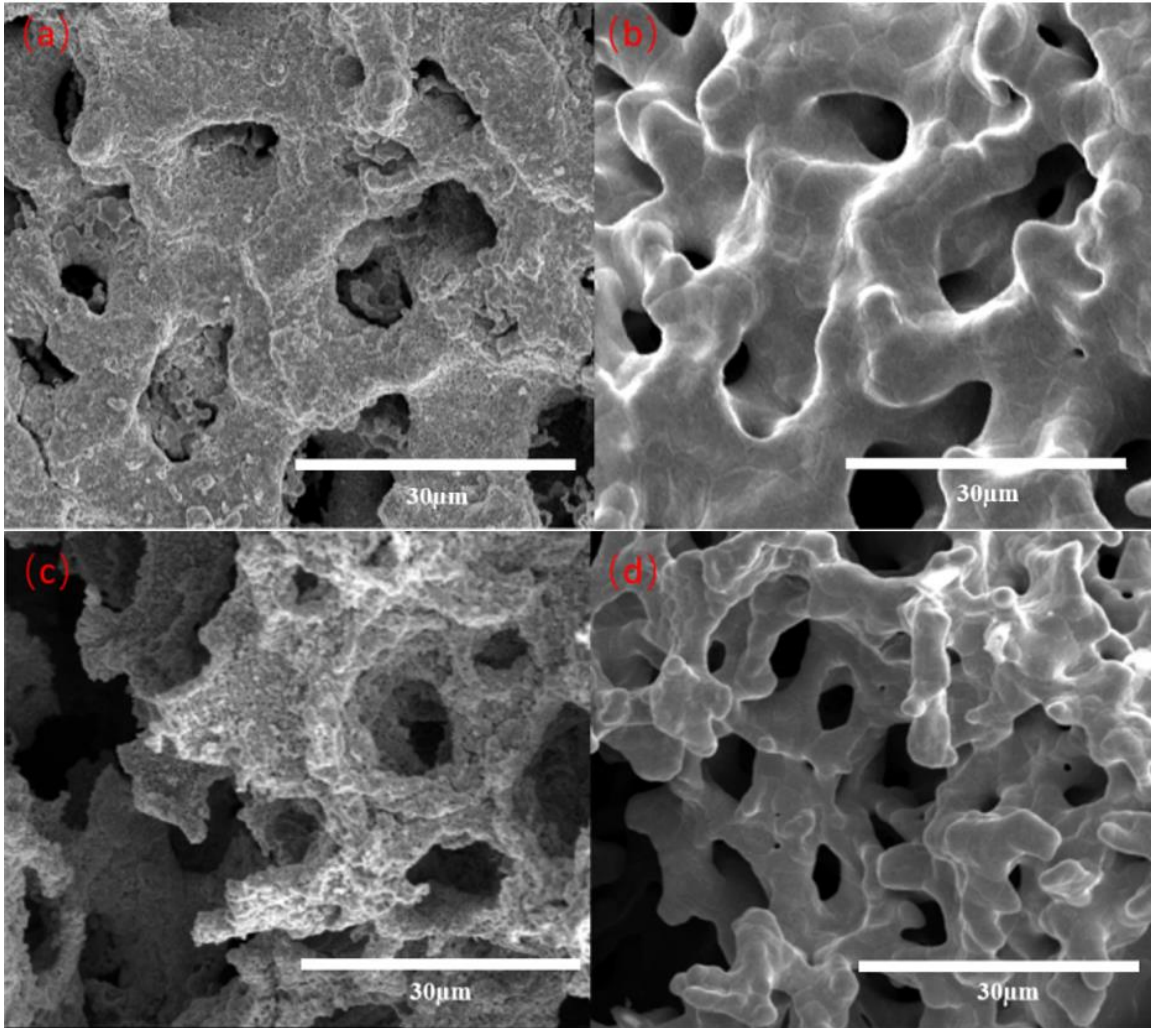


Figure 3.2, SEM image, (a) and (b) 46.8% Cu weight% bi-CuNi before and after the CVD of graphene; (c) and (d) 35.8% Cu weight% bi-CuNi before and after the CVD of graphene.

SEM is conducted to show the surface morphology of bi-CuNi. Figure 3.6 shows the SEM images of bi-CuNi and bi-CuNi-3DG. Figure 3.6 (a) and (b) are both from higher Cu concentration (46.8 weight%) bi-CuNi. Their bijel morphology are preserved. Figure 3.6 (c) and (d) are lower Cu concentration (35.8 weight%) bi-CuNi and its bi-CuNi-3DG, showing well-preserved bijel template morphology.

3.2.2 Raman spectra analysis and discussion

Raman spectra characterization is performed on bi-CuNi-3DG and biNi-3DG. It is acquired over at least 30 distinct points on each sample with a 50-micron spacing between measurements. Analysis is focused on the 2D intensity full width at half maximum (I_{2D} FWHM), 2D intensity (I_{2D}), and 2D /G ratio (I_{2D} / I_G). Raman data analyses of bi-CuNi-3DG are shown in Figure 3.8 (a–d). Figure 3.8 (a) and (c) are histograms that show I_{2D} full width at half maximum (FWHM) for bi-CuNi-3DG that have 35.8% and 46.8% Cu in their parent bi-CuNi, respectively. Turbostratic stacking may be identified by any of following cases: (a) Abnormally enhanced I_G intensity [84-85], (b) Abnormally high I_{2D} / I_G such as greater than 4 with narrow I_{2D} FWHM [86], (c) Combination Raman modes [42], (d) blueshifted I_{2D} peak position fit by a single Lorentzian with FWHM around 50 cm^{-1} [84,87].

In case (b), turbostratic stack graphene is likely to have narrow I_{2D} FWHM with width around 30 cm^{-1} , but Bernal stacked graphene will have I_{2D} wider FWHM, around 100 cm^{-1} [40-42]. In Figure 3.7(a-b), I_{2D} FWHM values range from 35–90 cm^{-1} with a high maximum probability density value between 50–55 cm^{-1} and average I_{2D} / I_G ratio of 0.78 ± 0.36 . In Figure 3.8(c-d), I_{2D} values range from 35–80 cm^{-1} with a high maximum probability density value between 50–55 cm^{-1} and average I_{2D} / I_G ratio of 1.18 ± 0.68 . What's more, in both samples, the I_{2D} FWHM center

around 50cm^{-1} . The data of I_{2D} / I_G and I_{2D} FWHM indicates a mixture of turbostratic and Bernal stacking in both samples. However, in Figure 3.8(c), there are less points at high I_{2D} FWHM and more points centered around 50cm^{-1} , indicating a greater turbostratic feature and better uniformity.

High 2D intensity values suggest the absence of Bernal stacking [42,73]. The 2D peak intensity values between the two samples are compared, showing the same result as I_{2D} FWHM analysis. The samples shown in Figure 3.8 (a) and (c) have average 2D intensity values of 826 ± 1200 and 504 ± 506 , respectively, indicating that graphene in Figure 3.8(c) has a lower Bernal stacking feature.

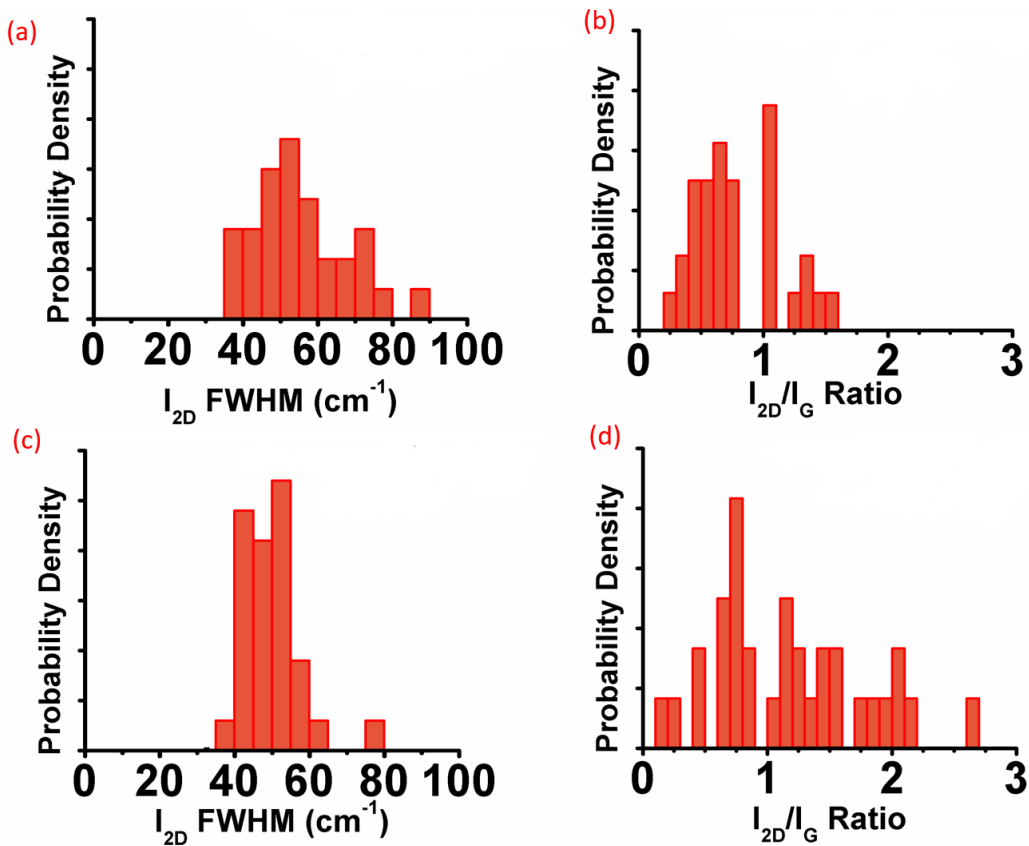


Figure 3.3, Raman spectra analysis histograms on bi-CuNi-3DG that have a Cu weight concentration of (a-b) 35.8%, (c-d) 46.8%, with average I_{2D} / I_G of 1.18 ± 0.68 and 0.78 ± 0.36 , respectively.

The Raman data analysis of biNi-3DG is shown in Figure 3.9; I_{2D} FWHM values range from 25–100 cm^{-1} with a high probability density value between 25–80 cm^{-1} , not centering around a small FWHM range but more evenly distributed, showing less uniformity in I_{2D} FWHM. Additionally, the variable layer thickness across the sample is shown by the I_{2D} / I_G . By comparing Figure 3.8 and Figure 3.9, it is obvious that with Cu in the metal template, the uniformity of the 3D graphene tends to be better.

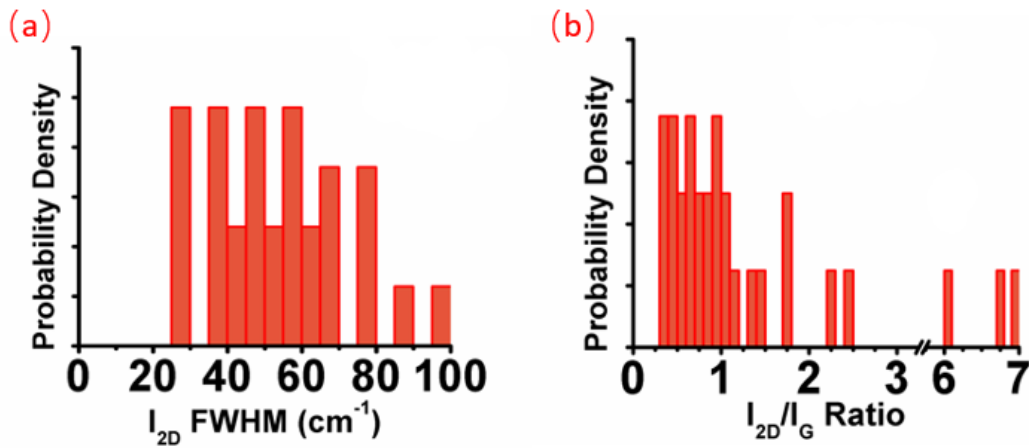


Figure 3.4, Raman spectra analysis histograms of biNi-3DG.

3.3 Conclusion

In this Chapter, bi-CuNi-3DG is produced from bi-CuNi with different Cu concentrations of 46.8% and 35.8%. They have I_{2D} / I_G of 1.18 ± 0.68 and 0.78 ± 0.36 , respectively, which implies that the more Cu concentration in the Cu-Ni alloy, the fewer the graphene layers; this result is consistent with the result of graphene on 2D Cu-Ni alloy films [28]. Furthermore, the biNi-3DG produced under same CVD growth parameters shows less uniformity in graphene

stacking mode, shown by both I_{2D} FWHM and I_{2D} / I_G , when comparing to that of bi-CuNi-3DG, indicating that the Cu-Ni alloy can successfully work as a controlling method in a 3D structure. More importantly, the bi-CuNi-3DG samples all show obvious turbostratic features—this is promising as a turbostratic stacking graphene shows similar electronic properties as an SLG [45]. Moreover, with the increase of the Cu concentration (from 35.8% to 46.8%) in their parent bi-CuNi, a greater turbostratic feature and better uniformity is shown in the bi-CuNi-3DG.

Chapter 4

Summary and future directions

4.1 Summary of the thesis

In this thesis, a method of producing bicontinuous Cu-Ni alloy (bi-CuNi) template is achieved by the electroless deposition of Cu and Ni on a bicontinuous PEGDA bijel template. Furthermore, by varying electroless deposition parameters of Cu, bi-CuNi with a Cu concentration of 46.8% and 35.8% are achieved. Using the same CVD growth parameters on both samples, Raman spectroscopy analyses show many regions exhibit a high 2D mode intensity, which increases with an increase in the Cu concentration in the alloy. The resultant 3D graphene from bi-CuNi via CVD (bi-CuNi-3DG) also exhibits turbostratic stacking in many regions of the sample.

In Chapter 2, the synthesis method of bi-CuNi is discussed. The synthesis of biNi is shown in 2.2.1, via an electroless deposition of Ni. The synthesis of bi-CuNi from biNi is shown in 2.2.2, via the electroless deposition of Cu, which is defined as a four-steps deposition as shown in Figure 2.5. Thereafter, the relationship between the deposited Cu thickness and experimental parameters (temperature, hole size of biNi) is estimated in 2.2.3. The morphology and Cu concentration analysis of bi-CuNi are conducted by SEM and EDS, proving that this

method can form Cu-Ni alloy with the bicontinuous morphology well preserved, as shown in Figure 2.8.

In Chapter 3, the CVD graphene growth on bi-CuNi and etched biNi is described. The porous morphology is well preserved in bi-CuNi-3DG, as shown in Figure 3.6. Furthermore, Raman spectra analysis is conducted. Graphene from 46.8% and 35.8% Cu concentration bi-CuNi have an average I_{2D} / I_G of 1.18 ± 0.68 and 0.78 ± 0.36 , respectively, indicating the higher Cu concentration in bi-CuNi scaffolds, the fewer the graphene layers. With Cu concentration of 46.8% and 35.8% in parent bi-CuNi, bi-CuNi-3DG with an obvious turbostratic stacking feature and good uniformity are achieved; the uniformity is better with the bi-CuNi-3DG from a 46.8% Cu concentration bi-CuNi template. Additionally, the bi-CuNi-3DG shows better uniformity than biNi-3DG, indicating that the use of Cu-Ni alloy is viable to control graphene growth on 3D structure.

4.2 Future directions

The future direction of the thesis is discussed herein. Future experiments should be conducted to determine a more precise control of Cu concentration in bi-CuNi and to explore alloys with higher Cu concentration. As shown in the calculation of electroless Cu deposition in 2.2.2, Cu concentration in bi-CuNi can be controlled using different electroless deposition temperatures or performing Cu deposition for more than one cycle. Figure 2.7 shows how much Cu can be deposited by one cycle of electroless deposition at different conditions, indicating that the precise control of Cu concentration in bi-CuNi is theoretically viable. Higher Cu concentration in bi-CuNi might be achieved with the porous structure being preserved; however, from former experience, when the Cu weight concentration is too high in bi-CuNi, the porous

morphology may be destroyed due to filling of pores. Figure 4.1 shows an example of the porous morphology being lost. In 2.2.2.1, HCl is used to etch the biNi to remove some Ni before the Cu electroless deposition, which turns out to be helpful in keeping the porous morphology. Thus, the concentration of HCl and etching time length are additional parameters that can be changed to determine a better etching condition.

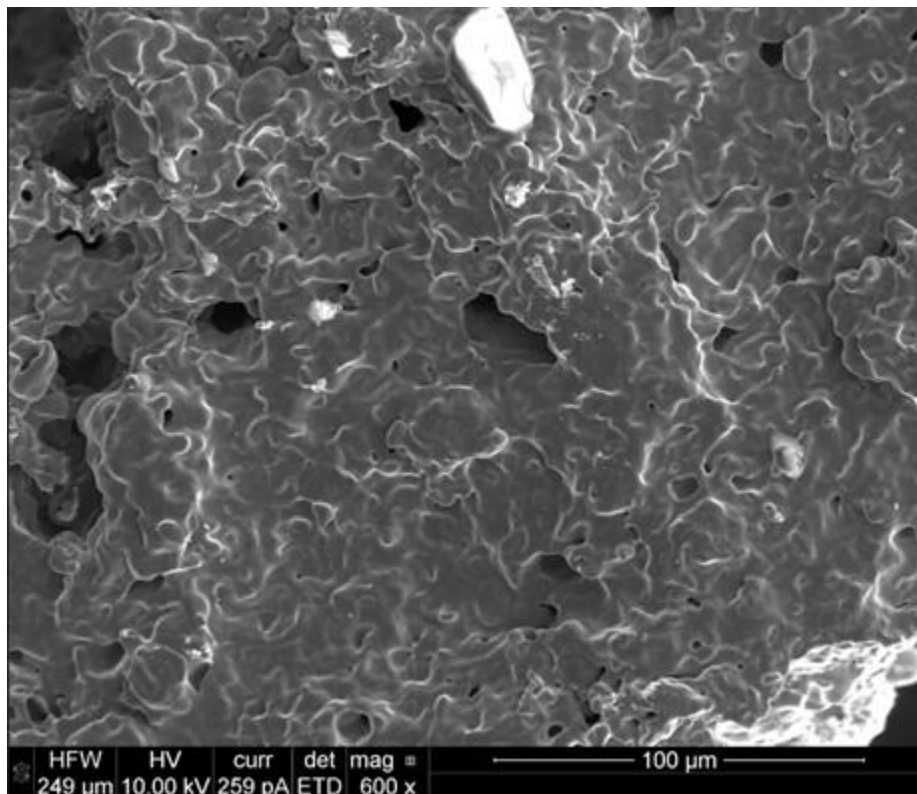


Figure 4.1, Graphene grown from 71.76 weight% bi-CuNi, morphology lost.

The goal of future experiments is to reach a higher Cu concentration and preserve the bicontinuous porous morphology. There are challenges that need to be addressed and solved to achieve this goal. For example, it is important to find biNi etching condition that preserves the stability of the scaffold; the biNi will be fragile if Ni is etched too thin. On the other hand, bi-CuNi won't have good porous morphology if biNi with thick Ni layers since the pores will be too small to accommodate additional thickness due to Cu deposition. Another challenge is to find

better Cu electroless deposition condition. Both Cu electroless deposition temperature and the number of electroless deposition cycles can influence the result. Additional experiments are required, to approach better experiment parameters, including biNi etching condition, Cu electroless deposition temperature, and the number of electroless deposition cycles.

Reference

- [1] T. Lin, I.W. Chen, F. Liu, C. Yang, H. Bi, F. Xu, F. Huang, Nitrogen-doped mesoporous carbon of extraordinary capacitance for electrochemical energy storage, *Science* 350(6267) (2015) 1508-1513.
- [2] Y. Ito, H.J. Qiu, T. Fujita, Y. Tanabe, K. Tanigaki, M. Chen, Bicontinuous Nanoporous N-doped Graphene for the Oxygen Reduction Reaction, 26(24) (2014) 4145-4150.
- [3] X. Dong, Y. Cao, J. Wang, M.B. Chan-Park, L. Wang, W. Huang, P. Chen, Hybrid structure of zinc oxide nanorods and three-dimensional graphene foam for supercapacitor and electrochemical sensor applications, *RSC Advances* 2(10) (2012) 4364.
- [4] C. Tang, B.-Q. Li, Q. Zhang, L. Zhu, H.-F. Wang, J.-L. Shi, F. Wei, CaO-Templated Growth of Hierarchical Porous Graphene for High-Power Lithium-Sulfur Battery Applications, 26(4) (2016) 577-585.
- [5] Z.-S. Wu, Y. Sun, Y.-Z. Tan, S. Yang, X. Feng, K. Müllen, Three-Dimensional Graphene-Based Macro- and Mesoporous Frameworks for High-Performance Electrochemical Capacitive Energy Storage, *Journal of the American Chemical Society* 134(48) (2012) 19532-19535.
- [6] H. Huang, T. Chen, X. Liu, H. Ma, Ultrasensitive and simultaneous detection of heavy metal ions based on three-dimensional graphene-carbon nanotubes hybrid electrode materials, 852 (2014) 45-54.
- [7] S. Bhaviripudi, X. Jia, M.S. Dresselhaus, J. Kong, Role of Kinetic Factors in Chemical Vapor Deposition Synthesis of Uniform Large Area Graphene Using Copper Catalyst, *Nano Letters* 10(10) (2010) 4128-4133.

- [8] A.N. Obraztsov, Making graphene on a large scale, *Nature Nanotechnology* 4(4) (2009) 212-213.
- [9] K.S. Kim, Y. Zhao, H. Jang, S.Y. Lee, J.M. Kim, K.S. Kim, J.-H. Ahn, P. Kim, J.-Y. Choi, B.H. Hong, Large-scale pattern growth of graphene films for stretchable transparent electrodes, *Nature* 457(7230) (2009) 706-710.
- [10] X. Li, W. Cai, J. An, S. Kim, J. Nah, D. Yang, R. Piner, A. Velamakanni, I. Jung, E. Tutuc, S.K. Banerjee, L. Colombo, R.S. Ruoff, Large-Area Synthesis of High-Quality and Uniform Graphene Films on Copper Foils, *Science* 324(5932) (2009) 1312-1314.
- [11] R. Muñoz, C. Gómez-Aleixandre, Review of CVD Synthesis of Graphene, 19(10-11-12) (2013) 297-322.
- [12] X. Li, W. Cai, L. Colombo, R.S. Ruoff, Evolution of Graphene Growth on Ni and Cu by Carbon Isotope Labeling, *Nano Letters* 9(12) (2009) 4268-4272.
- [13] S. Chen, W. Cai, R.D. Piner, J.W. Suk, Y. Wu, Y. Ren, J. Kang, R.S. Ruoff, Synthesis and Characterization of Large-Area Graphene and Graphite Films on Commercial Cu–Ni Alloy Foils, 11(9) (2011) 3519-3525.
- [14] F. García-Moreno, Commercial Applications of Metal Foams: Their Properties and Production, *Materials* 9(2) (2016) 85.
- [15] E. Wang, H. Wang, Z. Liu, R. Yuan, Y. Zhu, One-step fabrication of a nickel foam-based superhydrophobic and superoleophilic box for continuous oil–water separation, 50(13) (2015) 4707-4716.
- [16] Z. Chen, W. Ren, L. Gao, B. Liu, S. Pei, H.-M. Cheng, Three-dimensional flexible and conductive interconnected graphene networks grown by chemical vapour deposition, *Nature Materials* 10(6) (2011) 424-428.

- [17] M.N. Lee, A. Mohraz, Bicontinuous Macroporous Materials from Bijel Templates, *Advanced Materials* 22(43) (2010) 4836-4841.
- [18] K. Wang, Z. Li, Y. Wang, H. Liu, J. Chen, J. Holmes, H. Zhou, Carbon nanocages with nanographene shell for high-rate lithium ion batteries, *Advanced Materials* 22(43) (2010) 9748.
- [19] S. Torquato, S. Hyun, A. Donev, Multifunctional Composites: Optimizing Microstructures for Simultaneous Transport of Heat and Electricity, *Science* 297(5568) (2002) 958-962.
- [20] L. Lai, J.R. Potts, D. Zhan, L. Wang, C.K. Poh, C. Tang, H. Gong, Z. Shen, J. Lin, R.S. Ruoff, Exploration of the active center structure of nitrogen-doped graphene-based catalysts for oxygen reduction reaction, *Energy & Environmental Science* 5(7) (2012) 7936.
- [21] S. Stankovich, D.A. Dikin, G.H.B. Dommett, K.M. Kohlhaas, E.J. Zimney, E.A. Stach, R.D. Piner, S.T. Nguyen, R.S. Ruoff, Graphene-based composite materials, *Nature* 442(7100) (2006) 282-286.
- [22] T. Ramanathan, A.A. Abdala, S. Stankovich, D.A. Dikin, M. Herrera-Alonso, R.D. Piner, D.H. Adamson, H.C. Schniepp, X. Chen, R.S. Ruoff, S.T. Nguyen, I.A. Aksay, R.K. Prud'Homme, L.C. Brinson, Functionalized graphene sheets for polymer nanocomposites, *Nature Nanotechnology* 3(6) (2008) 327-331.
- [23] Z. Sun, Z. Yan, J. Yao, E. Beitler, Y. Zhu, J.M. Tour, Growth of graphene from solid carbon sources, *Science* 327(5923) (2010) 549-552.
- [24] Y. Zhang, L. Zhang, C. Zhou, Review of Chemical Vapor Deposition of Graphene and Related Applications, *Accounts of Chemical Research* 46(10) (2013) 2329-2339.
- [25] J.L. Q.K. Yu, S. Siripinglert, H. Li, Y.P. Chen, S. S. Pei, Graphene segregated on Ni surfaces and transferred to insulators, *Physics Research Publications*, Purdue University (2008).

- [26] A. Reina, X. Jia, J. Ho, D. Nezich, H. Son, V. Bulovic, M.S. Dresselhaus, J. Kong, Large Area, Few-Layer Graphene Films on Arbitrary Substrates by Chemical Vapor Deposition, *Nano Letters* 9(1) (2009) 30-35.
- [27] M. Losurdo, M.M. Giangregorio, P. Capezzuto, G. Bruno, Graphene CVD growth on copper and nickel: role of hydrogen in kinetics and structure, *Physical Chemistry Chemical Physics* 13(46) (2011) 20836.
- [28] X. Liu, L. Fu, N. Liu, T. Gao, Y. Zhang, L. Liao, Z. Liu, Segregation Growth of Graphene on Cu–Ni Alloy for Precise Layer Control, 115(24) (2011) 11976-11982.
- [29] Y.-Y. Lin, T.-H. Chu, C.-W. Chen, W.-F. Su, Improved performance of polymer/TiO₂ nanorod bulk heterojunction photovoltaic devices by interface modification, 92(5) (2008) 053312.
- [30] D.-W. Wang, F. Li, M. Liu, G.Q. Lu, H.-M. Cheng, 3D Aperiodic Hierarchical Porous Graphitic Carbon Material for High-Rate Electrochemical Capacitive Energy Storage, 47(2) (2008) 373-376.
- [31] C.M. Doherty, R.A. Caruso, B.M. Smarsly, C.J. Drummond, Colloidal Crystal Templating to Produce Hierarchically Porous LiFePO₄ Electrode Materials for High Power Lithium Ion Batteries, 21(13) (2009) 2895-2903.
- [32] Q. Yu, J. Lian, S. Siriponglert, H. Li, Y.P. Chen, S.-S. Pei, Graphene segregated on Ni surfaces and transferred to insulators, *Applied Physics Letters* 93(11) (2008) 113103.
- [33] L. Baraton, Z.B. He, C.S. Lee, C.S. Cojocaru, M. Châtelet, J.L. Maurice, Y.H. Lee, D. Pribat, On the mechanisms of precipitation of graphene on nickel thin films, 96(4) (2011) 46003.

- [34] H. Amara, J.M. Roussel, C. Bichara, J.P. Gaspard, F. Ducastelle, Tight-binding potential for atomistic simulations of carbon interacting with transition metals: Application to the Ni-C system, 79(1) (2009).
- [35] Y. Zhang, L. Gomez, F.N. Ishikawa, A. Madaria, K. Ryu, C. Wang, A. Badmaev, C. Zhou, Comparison of Graphene Growth on Single-Crystalline and Polycrystalline Ni by Chemical Vapor Deposition, 1(20) (2010) 3101-3107.
- [36] L. Tang, Y. Wang, Y. Li, H. Feng, J. Lu, J. Li, Preparation, Structure, and Electrochemical Properties of Reduced Graphene Sheet Films, Advanced Functional Materials 19(17) (2009) 2782-2789.
- [37] R.L. McCreery, Advanced Carbon Electrode Materials for Molecular Electrochemistry, Chemical Reviews 108(7) (2008) 2646-2687.
- [38] R.J. Lesuer, W.E. Geiger, Improved Electrochemistry in Low-Polarity Media Using Tetrakis(pentafluorophenyl)borate Salts as Supporting Electrolytes, 39(1) (2000) 248-250.
- [39] N.G. Shang, P. Papakonstantinou, M. McMullan, M. Chu, A. Stamboulis, A. Potenza, S.S. Dhesi, H. Marchetto, Catalyst-Free Efficient Growth, Orientation and Biosensing Properties of Multilayer Graphene Nanoflake Films with Sharp Edge Planes, 18(21) (2008) 3506-3514.
- [40] A. Luican, G. Li, A. Reina, J. Kong, R.R. Nair, K.S. Novoselov, A.K. Geim, E.Y. Andrei, Single-Layer Behavior and Its Breakdown in Twisted Graphene Layers, 106(12) (2011)
- [41] Z. Ni, Y. Wang, T. Yu, Y. You, Z. Shen, Reduction of Fermi velocity in folded graphene observed by resonance Raman spectroscopy, 77(23) (2008)
- [42] J.A. Garlow, L.K. Barrett, L. Wu, K. Kisslinger, Y. Zhu, J.F. Pulecio, Large-Area Growth of Turbostratic Graphene on Ni(111) via Physical Vapor Deposition, 6 (2016) 19804.

- [43] X. Du, I. Skachko, A. Barker, E.Y. Andrei, Approaching ballistic transport in suspended graphene, *Nature Nanotechnology* 3(8) (2008) 491-495.
- [44] K.F. Mak, M.Y. Sfeir, J.A. Misewich, T.F. Heinz, The evolution of electronic structure in few-layer graphene revealed by optical spectroscopy, 107(34) (2010) 14999-15004.
- [45] B. J. M, N.M.R. Peres, H. A, Graphene Bilayer with a Twist: Electronic Structure, 99(25) (2007).
- [46] C. Lee, X. Wei, J.W. Kysar, J. Hone, Measurement of the Elastic Properties and Intrinsic Strength of Monolayer Graphene, *Science* 321(5887) (2008) 385-388.
- [47] A.K. Geim, K.S. Novoselov, The rise of graphene, Co-Published with Macmillan Publishers Ltd, UK2009, pp. 11-19.
- [48] W. Bao, F. Miao, Z. Chen, H. Zhang, W. Jang, C. Dames, C.N. Lau, Controlled ripple texturing of suspended graphene and ultrathin graphite membranes, *Nature Nanotechnology* 4(9) (2009) 562-566.
- [49] J. Zang, S. Ryu, N. Pugno, Q. Wang, Q. Tu, M.J. Buehler, X. Zhao, Multifunctionality and control of the crumpling and unfolding of large-area graphene, *Nature Materials* 12(4) (2013) 321-325.
- [50] R.K. Joshi, P. Carbone, F.C. Wang, V.G. Kravets, Y. Su, I.V. Grigorieva, H.A. Wu, A.K. Geim, R.R. Nair, Precise and Ultrafast Molecular Sieving Through Graphene Oxide Membranes, *Science* 343(6172) (2014) 752-754.
- [51] Z. Qin, G.S. Jung, M.J. Kang, M.J. Buehler, The mechanics and design of a lightweight three-dimensional graphene assembly, *Science Advances* 3(1) (2017) e1601536.
- [52] B.G. Choi, M. Yang, W.H. Hong, J.W. Choi, Y.S. Huh, 3D Macroporous Graphene Frameworks for Supercapacitors with High Energy and Power Densities, 6(5) (2012) 4020-4028.

- [53] L.-S. Zhang, L.-Y. Jiang, H.-J. Yan, W.D. Wang, W. Wang, W.-G. Song, Y.-G. Guo, L.-J. Wan, Mono dispersed SnO₂ nanoparticles on both sides of single layer graphene sheets as anode materials in Li-ion batteries, 20(26) (2010) 5462.
- [54] H. Wang, L.-F. Cui, Y. Yang, H. Sanchez Casalongue, J.T. Robinson, Y. Liang, Y. Cui, H. Dai, Mn₃O₄–Graphene Hybrid as a High-Capacity Anode Material for Lithium Ion Batteries, Journal of the American Chemical Society 132(40) (2010) 13978-13980.
- [55] S.Q. Chen, Y. Wang, Microwave-assisted synthesis of a Co₃O₄–graphene sheet-on-sheet nanocomposite as a superior anode material for Li-ion batteries, 20(43) (2010) 9735.
- [56] Z.-S. Wu, G. Zhou, L.-C. Yin, W. Ren, F. Li, H.-M. Cheng, Graphene/metal oxide composite electrode materials for energy storage, Nano Energy 1(1) (2012) 107-131.
- [57] A. Morozan, B. Jousselme, S. Palacin, Low-platinum and platinum-free catalysts for the oxygen reduction reaction at fuel cell cathodes, 4(4) (2011) 1238.
- [58] Z.-S. Wu, S. Yang, Y. Sun, K. Parvez, X. Feng, K. Müllen, 3D Nitrogen-Doped Graphene Aerogel-Supported Fe₃O₄ Nanoparticles as Efficient Electrocatalysts for the Oxygen Reduction Reaction, Journal of the American Chemical Society 134(22) (2012) 9082-9085.
- [59] T. Gan, S. Hu, Electrochemical sensors based on graphene materials, 175(1-2) (2011) 1-19.
- [60] G. Lu, L.E. Ocola, J. Chen, Reduced graphene oxide for room-temperature gas sensors, Nanotechnology 20(44) (2009) 445502.
- [61] T. Wu, X. Zhang, Q. Yuan, J. Xue, G. Lu, Z. Liu, H. Wang, H. Wang, F. Ding, Q. Yu, X. Xie, M. Jiang, Fast growth of inch-sized single-crystalline graphene from a controlled single nucleus on Cu–Ni alloys, 15(1) (2015) 43-47
- [61] D. Li, M.B. Müller, S. Gilje, R.B. Kaner, G.G. Wallace, Processable aqueous dispersions of graphene nanosheets, Nature Nanotechnology 3(2) (2008) 101-105.

- [62] L.J. Cote, F. Kim, J. Huang, Langmuir–Blodgett Assembly of Graphite Oxide Single Layers, *Journal of the American Chemical Society* 131(3) (2009) 1043-1049.
- [63] J. Wu, S. Feng, X. Wei, J. Shen, W. Lu, H. Shi, K. Tao, S. Lu, T. Sun, L. Yu, C. Du, J. Miao, L.K. Norford, Facile Synthesis of 3D Graphene Flowers for Ultrasensitive and Highly Reversible Gas Sensing, *Advanced Functional Materials* 26(41) (2016) 7462-7469.
- [64] J. Filip, P. Kasák, J. Tkac, Graphene as signal amplifier for preparation of ultrasensitive electrochemical biosensors, *Chemical Papers* 69(1) (2015).
- [65] X. Dong, Y. Ma, G. Zhu, Y. Huang, J. Wang, M.B. Chan-Park, L. Wang, W. Huang, P. Chen, Synthesis of graphene–carbon nanotube hybrid foam and its use as a novel three-dimensional electrode for electrochemical sensing, *Journal of Materials Chemistry* 22(33) (2012) 17044.
- [66] E. Singh, Z. Chen, F. Houshmand, W. Ren, Y. Peles, H.-M. Cheng, N. Koratkar, Superhydrophobic Graphene Foams, *Small* 9(1) (2013) 75-80.
- [67] R. Muñoz, C. Gómez-Aleixandre, Review of CVD Synthesis of Graphene, *Chemical Vapor Deposition* 19(10-11-12) (2013) 297-322.
- [68] A.C. Ferrari, D.M. Basko, Raman spectroscopy as a versatile tool for studying the properties of graphene, *Nature Nanotechnology* 8(4) (2013) 235-246.
- [69] B. J. M, N.M.R. Peres, H. A, Graphene Bilayer with a Twist: Electronic Structure, 99(25) (2007).
- [70] A. Luican, G. Li, A. Reina, J. Kong, R.R. Nair, K.S. Novoselov, A.K. Geim, E.Y. Andrei, Single-Layer Behavior and Its Breakdown in Twisted Graphene Layers, 106(12) (2011).
- [71] S. Shallcross, S. Sharma, E. Kandelaki, O.A. Pankratov, Electronic structure of turbostratic graphene, 81(16) (2010).

- [72] K. Kim, S. Coh, L.Z. Tan, W. Regan, J.M. Yuk, E. Chatterjee, M.F. Crommie, M.L. Cohen, S.G. Louie, A. Zettl, Raman Spectroscopy Study of Rotated Double-Layer Graphene: Misorientation-Angle Dependence of Electronic Structure, 108(24) (2012).
- [73] A.C. Ferrari, J.C. Meyer, V. Scardaci, C. Casiraghi, M. Lazzeri, F. Mauri, S. Piscanec, D. Jiang, K.S. Novoselov, S. Roth, A.K. Geim, Raman Spectrum of Graphene and Graphene Layers, Physical Review Letters 97(18) (2006).
- [74] Y. Takesaki, K. Kawahara, H. Hibino, S. Okada, M. Tsuji, H. Ago, Highly Uniform Bilayer Graphene on Epitaxial Cu–Ni(111) Alloy, 28(13) (2016) 4583-4592.
- [75] W. Jiang, H. Xin, W. Li, Microcellular 3D graphene foam via chemical vapor deposition of electroless plated nickel foam templates, 162 (2016) 105-109.
- [76] J.-S. Lee, H.-J. Ahn, J.-C. Yoon, J.-H. Jang, Three-dimensional nano-foam of few-layer graphene grown by CVD for DSSC, 14(22) (2012) 7938.
- [77] Q. Ke, J. Wang, Graphene-based materials for supercapacitor electrodes – A review, Journal of Materiomics 2(1) (2016) 37-54.
- [78] H.W. Wanwei Jiang, Zhiwei Xu*, Nan Li, Cheng Chen, Cuiyu Li, Jing Li, Hanming Lv, Liyun Kuang, Xu Tian, A review on manifold synthetic and reprocessing methods of 3D porous graphene-based architecture for Li-ion anode, Chemical Engineering Journal (2018).
- [79] P. Poizot, S. Laruelle, S. Grugeon, L. Dupont, J.M. Tarascon, Nano-sized transition-metal oxides as negative-electrode materials for lithium-ion batteries, Nature 407(6803) (2000) 496-499.
- [80] Z. Sun, A.-R.O. Raji, Y. Zhu, C. Xiang, Z. Yan, C. Kittrell, E.L.G. Samuel, J.M. Tour, Large-Area Bernal-Stacked Bi-, Tri-, and Tetralayer Graphene, ACS Nano 6(11) (2012) 9790-9796.

- [81] S. Salimian, M.E. Azim Araghi, Manual turbostratic stacked graphene transistor: A study on electrical properties and device potential, 68 (2016) 28-36.
- [82] C. Shen, J. Liu, N. Jiao, C.X. Zhang, H. Xiao, R.Z. Wang, L.Z. Sun, Transport properties of graphene/metal planar junction, 378(18-19) (2014) 1321-1325.
- [83] F. Schwierz, J. Pezoldt, R. Granzner, Two-dimensional materials and their prospects in transistor electronics, 7(18) (2015) 8261-8283.
- [84] K. Kim, S. Coh, L.Z. Tan, W. Regan, J.M. Yuk, E. Chatterjee, M.F. Crommie, M.L. Cohen, S.G. Louie, A. Zettl, Raman Spectroscopy Study of Rotated Double-Layer Graphene: Misorientation-Angle Dependence of Electronic Structure, 108(24) (2012).
- [85] J.T. Robinson, J. Culbertson, M. Berg, T. Ohta, Work Function Variations in Twisted Graphene Layers, Scientific Reports 8(1) (2018).
- [86] U.M.R.D.R.P.C.N.G.U. Kulkarni, Highly Decoupled Graphene Multilayers: Turbostraticity at its Best, The Journal of Physical Chemistry Letters (2015), 6,21,4437-4443.
- [87] A.C. Ferrari, J.C. Meyer, V. Scardaci, C. Casiraghi, M. Lazzeri, F. Mauri, S. Piscanec, D. Jiang, K.S. Novoselov, S. Roth, A.K. Geim, Raman Spectrum of Graphene and Graphene Layers, Physical Review Letters 97(18) (2006).
- [88] K. S. Novoselov, A. K. Geim¹, S. V. Morozov, D. Jiang¹, Y. Zhang, S. V. Dubonos, I. V. Grigorieva, A. A. Firsov, Electric Field Effect in Atomically Thin Carbon Films, Science, (2004).